Journal of Nanobiotechnology

RESEARCH

Open Access

Exosomal miR-499a-5p from human umbilical cord mesenchymal stem cells attenuates liver fibrosis via targeting ETS1/GPX4-mediated ferroptosis in hepatic stellate cells

Zheng Wang[1†], Mengqin Yuan[2†], Lichao Yao[1], Zhiyu Xiong[1], Kai Dai[1], Pingji Liu[1], Ping Chen[1], Muhua Sun[1], Kan Shu[1], Yuchen Xia[3,4,5*] and Yingan Jiang[1*]

Abstract

Liver fibrosis is a leading cause of liver-related mortality worldwide, yet effective therapies remain limited. Mesenchymal stem cells (MSCs) have recently shown promise in treating liver fibrosis due to their anti-inflammatory and anti-fibrotic properties. However, the precise molecular mechanisms by which MSCs exert their effects remain unclear. In this study, we explored how human umbilical cord-derived mesenchymal stem cells (hUC-MSCs) contribute to treating liver fibrosis, and revealed a crucial role of ferroptosis in modulating hepatic stellate cells (HSCs) activity. We found that MSCs primarily promote ferroptosis in HSCs in an exosome-dependent manner. Specifically, MSC-derived exosomes (MSC-Exos) deliver miR-499a-5p, which interacts with the transcription factor ETS1, leading to the suppression of GPX4, a key regulator of ferroptosis, thereby reducing the fibrogenic activity of HSCs. Overexpression of ETS1 in HSCs counteracted miR-499a-5p-induced ferroptosis, underscoring the pathway's potential as a target for therapeutic intervention. Furthermore, molecular docking simulations further identified optimal ETS1-GPX4 binding sites. This research uncovers a novel mechanism by which MSCs may treat liver fibrosis, providing insights that could guide the development of more effective therapies for this widespread condition.

Introduction

Liver fibrosis is an abnormal repair process initiated by chronic and recurrent liver injury, which, if left unchecked, can develop into cirrhosis and eventually cause irreversible liver failure and hepatocellular carcinoma [1, 2]. Activation of hepatic stellate cells (HSCs) is a central mechanism of hepatic fibrosis. Driven by inflammatory mediators, HSCs differentiate into myofibroblasts, leading to excessive extracellular matrix deposition [3]. Additionally, activated HSCs secrete pro-inflammatory factors and chemokines, which recruit immune cells to sustain and amplify the inflammatory response [4]. Therefore, triggering apoptosis, promoting

†Zheng Wang and Mengqin Yuan contributed equally to this work and shared the first authorship.

*Correspondence:
Yuchen Xia
yuchenxia@whu.edu.cn
Yingan Jiang
jiangya_cn@aliyun.com

Full list of author information is available at the end of the article

Graphical Abstract

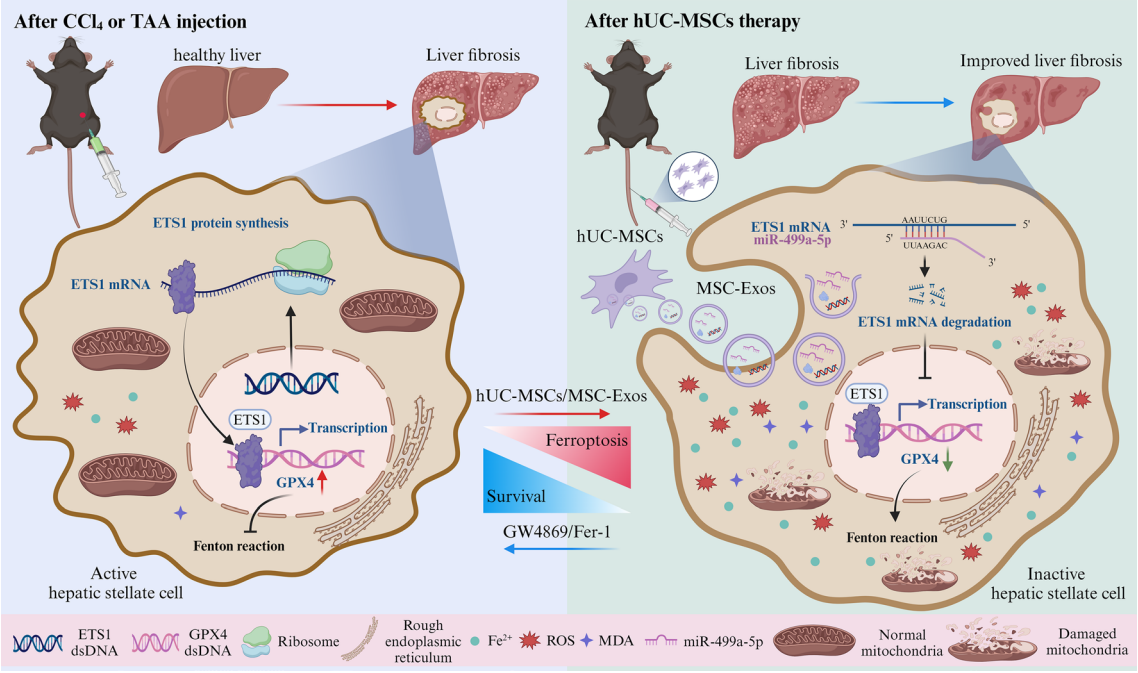

Keywords Liver fibrosis, Human umbilical cord mesenchymal stem cells, Ferroptosis, microRNA-499a-5p, ETS1

senescence, or deactivating activated HSCs is regarded as a viable therapeutic approach to slow down or reverse liver fibrosis progression [5].

Ferroptosis, a type of cell death distinct from apoptosis, has gained significant attention for its unique process, which involves lipid peroxidation and reactive oxygen species (ROS) buildup caused by intracellular iron accumulation [6]. As the central inhibitor of ferroptosis, glutathione peroxidase 4 (GPX4) serves an essential protective function by converting lipid hydroperoxides into harmless lipid alcohols. When GPX4 activity is diminished or lost, lipid peroxides accumulate in large quantities, ultimately triggering ferroptosis [7, 8]. Although these findings are informative, the exact contribution of ferroptosis to liver fibrosis progression is still uncertain. It is well-established that excessive iron accumulation in liver tissue poses a major risk for acute liver failure and fibrosis development [9, 10]. Notably, recent studies suggest that certain compounds, such as isoliquiritigenin, esculin, and sorafenib, could mitigate liver fibrosis by triggering ferroptosis in HSCs, which implies that selectively inducing ferroptosis in HSCs, while avoiding damage to healthy hepatocytes, could be a promising therapeutic strategy [11–13].

Mesenchymal stem cells (MSCs), particularly those derived from human umbilical cords (hUC-MSCs), have garnered considerable attention because of their capacity to modulate the microenvironment, exert anti-inflammatory effects, and promote tissue regeneration [14, 15]. Interestingly, the regulatory effects of MSCs on different cell types within a tissue can vary significantly, depending on specific microenvironmental cues and cellular interactions [16]. Such differential interactions between MSCs and various liver cell types create a unique therapeutic window where MSCs could selectively prevent apoptosis of hepatocytes and inhibit HSC activation. The regulatory role of MSCs in regulating ferroptosis is well documented [17]. For example, MSCs could promote the recovery of carbon tetrachloride (CCl_4)-induced acute liver injury by alleviating hepatocyte ferroptosis [18]. However, whether MSCs can leverage this interaction to induce ferroptosis specifically in HSCs as a means to treat liver fibrosis remains largely unknown.

This study aimed to explore how hUC-MSCs induce ferroptosis in HSCs and the associated mechanisms. Our findings demonstrate that hUC-MSCs exhibit antifibrotic properties by promoting ferroptosis and inactivating HSCs via exosome-mediated delivery of miR-499a-5p, which targets the ETS1/GPX4 signaling pathway. These findings reveal a novel antifibrotic mechanism of hUC-MSCs, offering a promising strategy for treating liver fibrosis.

Materials and methods

Animals in vivo study

Six-week-old male C57/BL6 mice were sourced from Vital River Laboratory Animal Technology Co., Ltd. (Beijing, China). The study protocol received approval from the Animal Ethics Committee of Renmin Hospital of Wuhan University, Wuhan, China (Permit No. SYXK(E) 2020-0027), in strict accordance with their guidelines (Approval Nos. 20220901 A, 20230103 C). The mice were maintained in a specific pathogen-free barrier facility, provided with a 12-hour light/dark cycle and ad libitum access to standard laboratory chow. Liver fibrosis was induced using previously published protocols with CCl_4 (#289116, Sigma) or TAA (thioacetamide, #163678, Sigma) [19, 20]. Following a one-week acclimation, the mice were arbitrarily divided into Control, liver fibrosis, and MSCs groups ($n = 6$ per group). Mice in the CCl_4 and CCl_4 + MSCs groups were given intraperitoneal injections of 10% CCl_4 (1.0 ml/kg) twice a week for 12 weeks. Similarly, the TAA and TAA + MSCs groups received TAA (200 mg/kg) via intraperitoneal injection on the same schedule, while Control mice were injected with an equal volume of saline. Beginning in the 8th week, the MSCs group received tail vein injections of 1 × 10^6 second-passage MSCs weekly for 5 weeks. For the exosome group, starting from the 8th week, mice were administered MSC-exosomes (MSC-Exos) at 25 mg/kg body weight for 5 weeks ($n = 6$) [21]. 48 h after the final MSCs and MSC-Exos injection, mice were sacrificed, and serum along with liver samples were harvested for further analysis.

Liver histological analysis

Mouse liver tissues were fixed in 4% paraformaldehyde, embedded in paraffin, and sectioned. H&E, Masson, and Sirius Red staining were performed to evaluate tissue architecture and collagen fibers. For immunohistochemistry, sections were incubated with primary antibodies targeting α-SMA, Col1a1, and Gpx4, followed by HRP-conjugated secondary antibodies and DAB-based visualization. Images were captured via light microscopy. Antibody details are in Tab. S1.

In vivo and ex vivo fluorescence imaging of DiR-labeled MSCs in liver fibrosis and control mice

DiR was used as a fluorescent marker to label MSCs in vitro for 30 min, following established protocols [22]. The labeled cells were injected into the tail veins of Control and CCl_4 group mice, each receiving 1 × 10^6 cells ($n = 3$ per group). To track the cells in vivo, mice were anesthetized with 1% pentobarbital and shaved 24 h after model establishment. Fluorescence and X-ray imaging were conducted using the Bruker MS FX Pro system. To assess organ tropism, key organs (heart, spleen, liver, lungs, kidneys, and intestine) were imaged ex vivo following euthanasia by cervical dislocation. The organs were rapidly harvested and placed in Petri dishes for fluorescence imaging. Parameters including exposure time, aperture, sample positioning, and pixel settings were controlled to ensure consistent imaging results.

Cell culture conditions and drug treatment

MSCs were sourced from Shenzhen Wingor Biological Co., Ltd. mHSCs were sourced from iCell Bioscience Inc., and LX-2 cells were acquired from Wuhan Pricella Biotechnology Co., Ltd. MSCs were cultured in serum-free mesenchymal stem cell medium. mHSCs were cultured in RPMI 1640, while LX-2 cells were maintained in high-glucose DMEM; both media contained 10% fetal bovine serum and 1% penicillin/streptomycin. All cell cultures were maintained at 37 °C in a 5% CO_2 atmosphere. A Transwell system was employed to examine the effects of passage 2 to 5 MSCs on mHSCs and LX-2 cells. After 48 h of co-culturing, the cells were collected for further analysis. Ferrostatin-1 (Fer-1, #HY-100579, MCE), Erastin (Eras, #HY-15763, MCE) and exosome inhibitor GW4869 (#HY-19363, MCE) were dissolved in DMSO for experiments.

Differentiation potential of MSCs

MSCs were subjected to trilineage differentiation using adipogenic, osteogenic, and chondrogenic induction media (#PD-019, #PD-017, #PD-018), all provided by Wuhan Pricella Biotechnology Co., Ltd. All procedures were strictly performed following the respective product manuals.

Characterization of MSCs by flow cytometry

Flow cytometry characterized MSCs surface markers. Cells were digested, centrifuged, and resuspended in PBS before incubation with primary antibodies, including CD90, CD73, CD105, HLA-DR, CD34, and CD45, for 30 min. After washing, fluorescent secondary antibodies were added and incubated at 37 °C for 30 min. Cells were then washed, resuspended, and analyzed via Beckman Coulter CytoFlex, with data processed using FlowJo software. Details of the antibodies are provided in Tab. S1.

Isolation and characterization of MSC-Exos

MSC-Exos were prepared by ultracentrifugation, following established methods [23]. Transmission electron microscopy observed exosome morphology, while the nano analyzer (NanoFCM, N30E) measured size and concentration. Western blotting detected the expression of CD9, TSG101, and Calnexin, with MSCs as the control group. MSC-Exos were filtered through a 0.22 μm membrane to ensure sterility before being used for cell treatments (400 μg/mL). Antibody details are listed in Tab. S1.

Uptake of PKH26-labeled MSC-Exos

MSC-Exos were labeled with PKH26 (#HY-D1451, MCE), incubated with mHSCs and LX-2 cells for 24 h, and their intracellular localization was determined via confocal microscopy.

Cell counting kit-8 (CCK-8) cell viability measurement

HSCs were plated in 96-well plates at 3000 cells per well, treated with MSCs conditioned medium (MSCs-CM), Fer-1 (1 μM), and Eras (10 μM) for 48 h, then incubated with CCK-8 reagent for 1 h before measuring OD at 450 nm.

mRNA sequencing, miRNA sequencing, and bioinformatics analysis

Total RNA was extracted from the mouse liver using Trizol, followed by cDNA library preparation and sequencing on the DNBSEQ platform. DESeq2 was used to identify differentially expressed genes (DEGs) among the Control, CCl_4, and CCl_4 + MSCs groups, with criteria of $|\log_2 \text{FoldChange}| > 0.585$ and Q value < 0.05. Volcano plots and heatmaps were created using the "ggplot2" and "pheatmap" R packages. GO and KEGG enrichment analyses were performed via "clusterProfiler".

The GSE229291 dataset, providing RNA profiles of activated and quiescent HSCs (aHSCs and qHSCs) from a liver fibrosis mouse model, was acquired from the GEO database [24]. The GSE14323 dataset, including data from healthy controls and liver cirrhosis patients, was also accessed via the GEO database [25]. The 2023 update of the ferroptosis database (FerrDb V2) identified 564 ferroptosis gene regulators, comprising drivers, suppressors, markers, and unclassified genes [26].

Total miRNA from mHSCs was extracted using Trizol, followed by enrichment and identification. The enriched small RNAs were reverse-transcribed into cDNA and subjected to quality control. High-throughput sequencing was conducted on the Illumina NovaSeq platform. Following sequencing and target gene prediction, functional enrichment analysis was performed with the R package "clusterProfiler".

Measurement of Fe^{2+} and malondialdehyde (MDA) levels

Intracellular Fe^{2+} levels in HSCs were measured with the Fe^{2+} Assay Kit (#E-BC-K881-M, Elabscience), and MDA levels were quantified using the MDA Assay Kit (#E-BC-K028-M, Elabscience). In liver tissue, SOD activity was determined using the Total Superoxide Dismutase (T-SOD) Assay Kit (#A001-1, Nanjing Jiancheng), and MDA levels was analyzed with the MDA Assay Kit (#G4302, Servicebio). Serum iron levels in mice were determined using the Serum Iron Assay Kit (#A039-1-1, Nanjing Jiancheng). All assays followed the manufacturer's protocols.

BODIPY fluorescence staining

Thawed liver sections were incubated with BODIPY dye for 20 min, followed by a 10-minute DAPI counterstain, mounted, and then observed under a fluorescence microscope.

ROS measurement and mitochondrial membrane potential assay

ROS levels and mitochondrial membrane potential in HSCs were measured following the manufacturer's protocols using the ROS Assay Kit (#S0033S) and the JC-1 Assay Kit (#C2006), both from Beyotime.

Transmission electron microscopy (TEM) of HSCs

After a 4-hour fixation, cells were embedded in 1% agarose, dehydrated, and sectioned into 60–90 nm ultrathin slices. Transmission electron microscopy was used to image the sections after staining with uranyl acetate and lead citrate.

RNA isolation, cDNA synthesis, and qRT-PCR evaluation

Total RNA from cells and tissues was extracted with the RNA Extraction Kit (#RN2802, Aidlab). RNA was reverse transcribed into cDNA using the ABScript III RT Master Mix (#RK20429, ABclonal). Intracellular miRNA was extracted using the miRNA Extraction Kit (#RN0501, Aidlab). miRNA from MSC-Exos was extracted using the miEASYspin Universal microRNA Kit (#RN5901, Aidlab). First-strand cDNA was synthesized using the ABScript miRNA First-Strand Synthesis Kit (#RK30170, ABclonal). qRT-PCR experiments were conducted with the SYBR Green Fast qPCR Mix (#RK21203, ABclonal). All qRT-PCR reactions were performed on the Roche Lightcycler 4800II, with ACTB and U6 as reference genes for normalization. The synthetic cel-miR-39 was used as an exogenous reference control to confirm the presence of hsa-miR-499a-5p in exosomes. Primer sequences are listed in Tab. S2.

Western blotting (WB) analysis

Proteins from mouse liver tissues and cell samples were extracted using RIPA buffer with PMSF and Cocktail, and quantified with a BCA assay. After SDS-PAGE separation and transfer to PVDF membranes, the membranes were blocked with 5% skim milk, followed by overnight incubation with primary antibodies at 4 °C. The next day, membranes were treated with HRP-conjugated secondary antibodies and visualized by chemiluminescence. Relative protein expression was analyzed using ImageJ. Antibody details are listed in Tab. S1.

Serum inflammatory cytokine and liver function marker assays

Interleukin-6 (IL-6, #ELK1157MS), tumor necrosis factor-α (TNF-α, #ELK1387MS), interleukin-10 (IL-10, #ELK1143) and interleukin-1β (IL-1β, #ELK1271MS) levels in mouse serum were quantitatively analyzed using ELISA kits (ELK Biotechnology). Serum concentrations of alanine aminotransferase (ALT), aspartate aminotransferase (AST), alkaline phosphatase (ALP), and albumin (ALB) were also measured using an automated biochemical analyzer.

Immunofluorescence analysis

Liver sections were fixed, permeabilized, and blocked before overnight incubation with primary antibodies. After washing, fluorescent secondary antibodies and DAPI staining were applied for fluorescence microscopy analysis. Antibody details are listed in Tab. S1.

Small interfering RNA (siRNA) and miRNA mimic transfection

Human GPX4 siRNA and mouse Gpx4 siRNA were obtained from Shanghai DesignGene Biotechnology Co., Ltd. Human ETS1 siRNA and mouse Ets1 siRNA were sourced from Haixing Bioscience (Suzhou, China). miRNA mimic was obtained from GenePharma (Shanghai, China). HSCs were transfected with siRNA (0.1 μM) using Lipofectamine™ 2000 (#11668019, Invitrogen) and miRNA mimic (0.1 μM) using Lipofectamine™ RNAiMAX (#13778100, Invitrogen). The medium was replaced after 6 h, and RNA or protein was extracted 48 h post-transfection for analysis. siRNA sequences are listed in Tab. S3 and miRNA mimic sequences are provided in Tab. S4.

Dual-luciferase reporter assay

To examine the regulatory effect of miR-499a-5p on ETS1, 3' UTR sequences of ETS1 with wild-type (WT) or mutant (MuT) binding sites were inserted into pGL6 vectors, generating pGL6-ETS1-WT and pGL6-ETS1-MuT. LX-2 cells were co-transfected with these constructs, miR-499a-5p mimic or NC mimic, and pRL-TK using Lipofectamine 2000. Additionally, the effect of ETS1 on GPX4 promoter activity was tested by co-transfecting cells with pGL3-GPX4-Promoter or pGL3-Basic, and pcDNA3.1-ETS1 or its control. Luciferase activities were measured 24 h later using the Dual-Luciferase Reporter Assay System, with firefly luciferase normalized to Renilla.

ChIP-qPCR

LX-2 cells were crosslinked with 1% formaldehyde, and the reaction was stopped with glycine. After lysis and sonication, protein-DNA complexes were immunoprecipitated using magnetic beads. Following washing and elution, the crosslinks were reversed, and the DNA was quantified by qPCR with primers from Tab. S5.

Establishment of human and mouse ETS1-Overexpressing cell lines

The human pHBLV-h-ETS1-3×Flag-ZsGreen-puro and empty pHBLV-h-ZsGreen-puro lentiviral vectors were obtained from Hanbio Tech (Shanghai, China). LX-2 cells were exposed to lentivirus (MOI 15) in DMEM with 7 μg/mL Polybrene. Stable human ETS1-overexpressing LX-2 cell lines were selected using puromycin (1 μg/mL). The mouse pHBLV-m-Ets1-3×flag-ZsGreen-puro and empty pHBLV-m-ZsGreen-puro lentiviral vectors were also obtained from Hanbio Tech (Shanghai, China). mHSCs were exposed to lentivirus (MOI 30) in RPMI 1640 with 6 μg/mL Polybrene, and stable Ets1-overexpressing mHSCs lines were selected with puromycin (3 μg/mL). Empty vector cells (EV) and ETS1-overexpressing cells (OE ETS1) were used for subsequent experiments.

Molecular Docking analysis of ETS1 and GPX4 promoter

Molecular docking was conducted to examine the interaction patterns between ETS1 and the GPX4 promoter sequence. Protein sequence data for human ETS1 was retrieved from the UniProt database, and its structure was obtained from the PDBe database (PDBe ID: 1gvj). A 2000-base pair upstream sequence from the GPX4 gene's transcription start site was extracted from the NCBI database for promoter region analysis. In the molecular docking experiments, ETS1's 3D structure was used as the receptor, and the GPX4 promoter sequence was modeled as the ligand. Docking computations were conducted using HDOCK software, with the CREATEPL module used to construct the ETS1-GPX4 complex model. The resulting complex model was then analyzed and visualized using PyMOL software to elucidate the binding characteristics.

Statistical analyses

Data are expressed as mean ± standard error of the mean (SEM). Statistical analysis was performed using t-tests or one-way ANOVA to evaluate significant differences. The analysis was conducted using GraphPad Prism 8.0. Significance between groups is indicated as follows: $^{*}P < 0.05$, $^{**}P < 0.01$, $^{***}P < 0.001$, $^{****}P < 0.0001$.

Results

MSCs mitigate liver fibrosis induced by CCl_4 and TAA in mice

To verify the multidirectional differentiation potential of the purchased MSCs and characterize their phenotypes, several in vitro experiments were performed. Oil

red O, alizarin red and alcian blue staining confirmed adipogenic, osteogenic and chondrogenic differentiation, respectively, indicating successful lineage-specific differentiation (Fig. S1A-C). Flow cytometry further validated the MSC phenotype by confirming positive markers (CD73, CD90, CD105) and negative markers (CD34, CD45, HLA-DR) (Fig. S1D-E). These results uniformly confirmed the MSC characteristics of the cells.

Two well-characterized mouse models of liver fibrosis were generated using CCl_4 and TAA injections. The timeline for the CCl_4-induced mouse model and MSC administration is shown in Fig. 1A. The CCl_4 group exhibited a decrease in body weight compared to Controls, while the MSC group showed a noticeable increase relative to the CCl_4 group (Fig. 1B). To verify MSC homing to the liver, immunofluorescence staining for CD73 and CD90 was performed on liver tissues. The liver tissues of MSC-treated mice exhibited significantly elevated levels of CD73 and CD90 compared to the Control and CCl_4 groups, indicating successful MSC homing to the liver (Fig. 1C). In vivo fluorescence imaging revealed the presence of DiR-labeled MSCs in the livers of both Control mice and those with CCl_4-induced liver fibrosis. Ex vivo fluorescence imaging revealed significant MSC accumulation in the lungs, with detectable distribution in the liver and spleen, but no significant DiR signals in the heart, kidneys, or intestines. The liver of fibrotic mice exhibited stronger fluorescence signals, indicating that MSCs have an enhanced propensity to migrate toward damaged tissues under pathological conditions (Fig. 1D). Gross liver examination revealed shrinkage and a granular surface in the CCl_4 group, in contrast to the Control, whereas the MSC group displayed reduced granularity and a smoother surface (Fig. 1E). H&E staining revealed that MSC treatment markedly improved CCl_4-induced hepatocyte structural disarray and perivascular inflammatory cell infiltration. A reduction in collagen fibers and fibrosis was observed following MSC treatment, as shown by Masson and Sirius red staining (Fig. 1F, Fig. S1F). Immunohistochemical analysis revealed elevated levels of α-SMA and Col1a1 in the CCl_4 group, which decreased following MSC treatment (Fig. 1G, Fig. S1G). Blood biochemical analysis revealed substantial reductions in the levels of ALT, AST, and ALP, alongside an increase in ALB, indicating improved liver function following MSC treatment (Fig. 1H). MSC treatment downregulated the expression of α-SMA, Tgfb1, Desmin, and Vimentin in mice exposed to CCl_4 (Fig. 1I-J).

The timeline for the TAA-induced mouse model and MSC treatment schedule is illustrated in Fig. S2A. Gross liver examination, histopathology, immunohistochemistry, biochemical assays, ELISA, qRT-PCR, and Western blot results demonstrated the alleviation of liver fibrosis by MSCs (Fig. S2B-H, Fig. S1H-I). In summary, MSCs mitigate liver fibrosis induced by CCl_4 and TAA in mice.

MSCs inhibit ferroptosis in liver fibrotic tissues

Comprehensive gene expression profiling of liver tissue samples from Control, CCl_4-induced liver fibrosis, and MSCs-treated groups was conducted using RNA sequencing to deepen the understanding of the therapeutic mechanisms of MSCs. Initially, a comparison between the CCl_4 -induced fibrosis group and the normal Control identified 1,846 significantly upregulated and 1,767 significantly downregulated genes. After MSC treatment, 2,019 genes were upregulated and 2,056 genes were downregulated compared to the CCl_4-induced fibrosis group. Notably, 1,162 downregulated and 1,233 upregulated genes induced by CCl_4 were reversed by MSC treatment, suggesting these DEGs may play crucial roles in MSCs' therapeutic effects (Fig. 2A). Subsequently, genes with significant expression differences across the three groups were visualized using heatmaps (Fig. 2B). Further GO analysis showed that these 2,395 DEGs were notably enriched in processes associated with oxidative stress response, and iron ion binding (Fig. 2C). KEGG pathway analysis suggested that these DEGs were involved in metabolic pathways, glutathione metabolism, and ferroptosis (Fig. 2D).

Protein assays for oxidative stress and ferroptosis markers were conducted in mouse liver tissues. Results indicated a significant upregulation of Cox2 and a notable downregulation of Sod1 protein expression in the liver fibrosis model group. These changes were significantly reversed by MSC treatment (Fig. 2E). Serum iron levels, along with SOD and MDA in liver tissues, were also measured. Fibrotic mice exhibited elevated serum iron and MDA levels, with decreased SOD levels compared to Controls. MSC treatment reduced serum iron and MDA levels while increasing SOD levels (Fig. 2F-H). BODIPY fluorescence staining revealed a higher lipid peroxidation level in fibrotic tissues compared to the Control group, demonstrated by increased fluorescence intensity, while MSC treatment significantly reduced lipid peroxidation (Fig. 2I). Collectively, these results suggest that MSCs may exert their effects by modulating ferroptosis in fibrotic tissue.

MSCs inhibit HSCs activation by inducing ferroptosis

Although previous studies have shown that MSCs protect against acute liver injury by inhibiting hepatocyte ferroptosis, their effect on HSC ferroptosis remains unclear [18]. Considering the central role of HSCs in liver fibrosis and the growing recognition of ferroptosis in cell fate regulation, it is essential to determine whether MSCs can influence ferroptosis in HSCs. Hence, we investigated

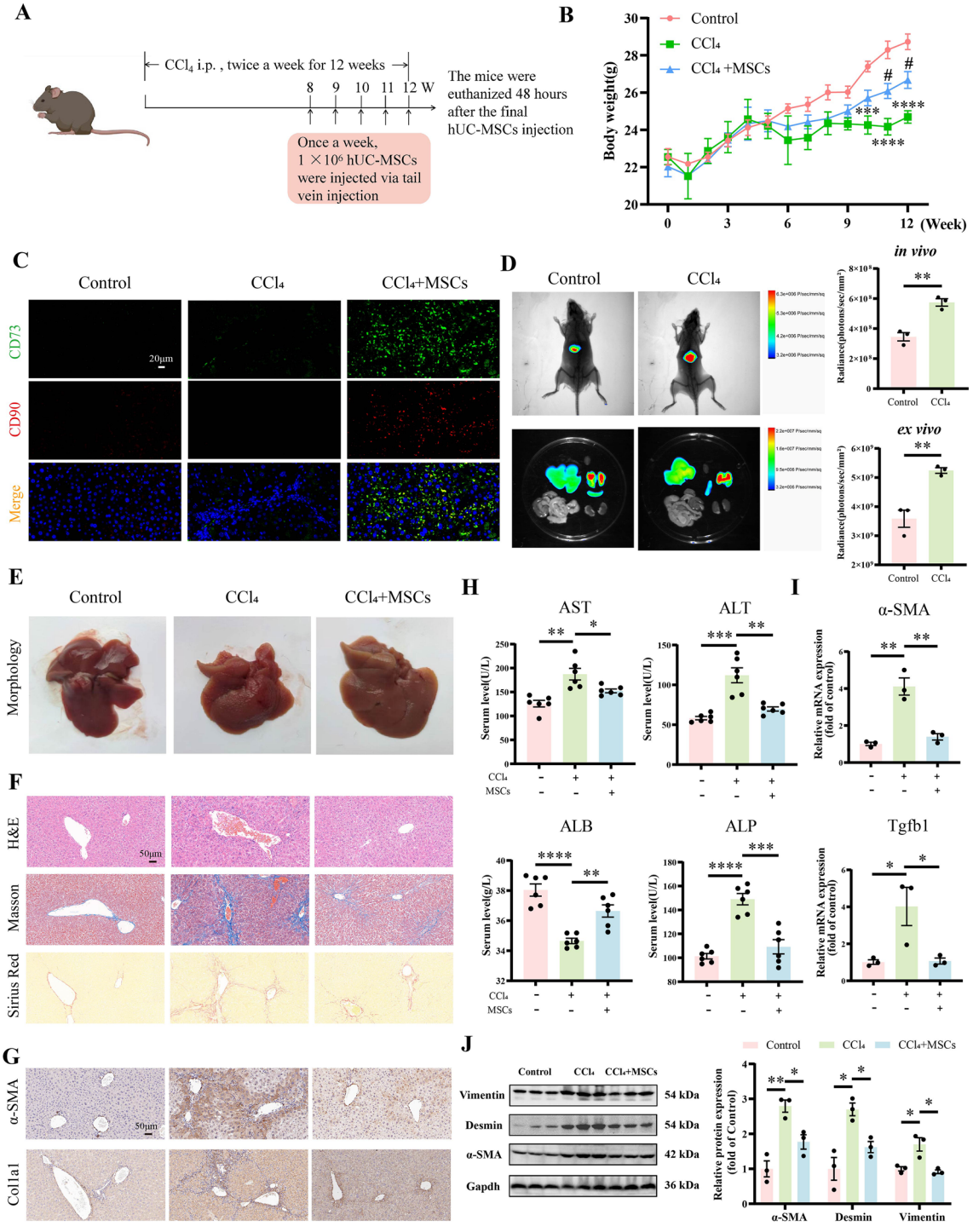

Fig. 1 MSC treatment mitigates CCl_4-induced liver fibrosis. (**A**) Schematic of the CCl_4 modeling timeline. (**B**) Body weight changes in Control, CCl_4, and CCl_4 + MSCs groups. ***$P < 0.001$, CCl_4 vs. Control group, ****$P < 0.0001$, CCl_4 vs. Control group; # $P < 0.05$, CCl_4 + MSCs vs. CCl_4 group. (**C**) Immunofluorescence staining of CD73 and CD90 in liver tissue. Scale bar = 20 μm. (**D**) In vivo imaging of DiR-labeled MSCs 24 h post-injection in mice and ex vivo fluorescence imaging of liver, heart, lungs, spleen, kidneys, and intestines. (**E**) Representative liver morphology in the three groups. (**F**) Liver sections were stained with H&E, Masson, and Sirius Red in the three groups. Scale bar = 50 μm. (**G**) Immunohistochemical staining of α-SMA and Col1a1 in liver sections. Scale bar = 50 μm. (**H**) Liver function tests for serum ALT, AST, ALP, and ALB levels in the mouse groups. (**I**) qRT-PCR analysis of α-SMA and Tgfb1 mRNA expression in liver tissues. (**J**) Western blot analysis of α-SMA, Desmin, and Vimentin protein expression in liver tissues. The data are presented as the mean ± SEM from at least three independent experiments. *$P < 0.05$, **$P < 0.01$, ***$P < 0.001$, ****$P < 0.0001$ indicate significant differences between the indicated groups

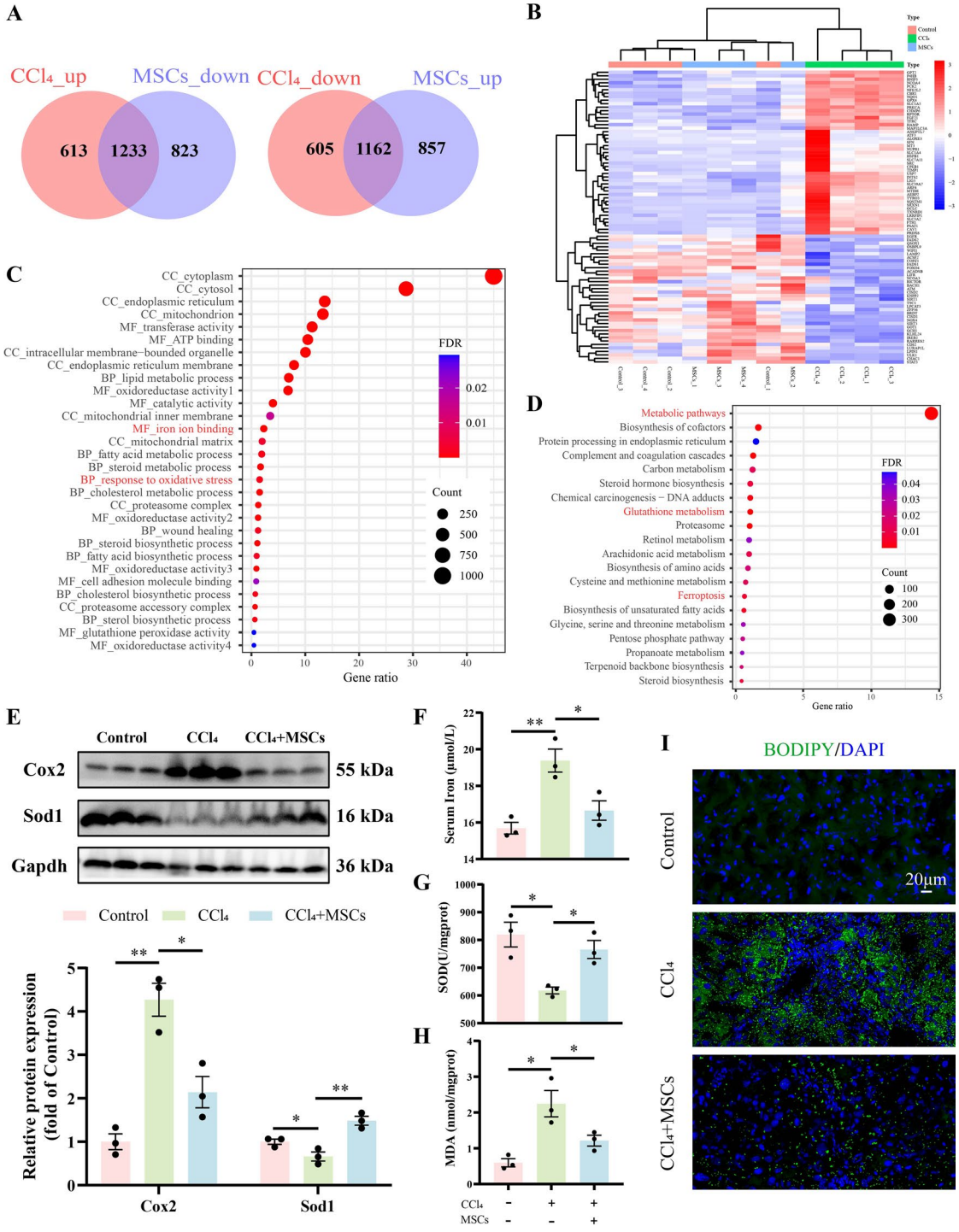

Fig. 2 Ferroptosis in liver fibrotic tissues is inhibited by MSCs. (**A**) Venn diagram identifying DEGs associated with MSC treatment. (**B**) Heatmap of RNA sequencing results from Control, CCl_4, and CCl_4 + MSC groups. (**C**) GO analysis of DEGs modulated by MSCs. (**D**) KEGG analysis of DEGs modulated by MSCs. (**E**) Western blot of Cox2 and Sod1 expression in liver tissues. (**F**) Serum iron levels measurement. (**G**) SOD levels measurement in liver tissues. (**H**) MDA levels measurement in liver tissues. (**I**) Immunofluorescence staining of BODIPY in liver tissue. Scale bar = 20 μm. The data are presented as the mean ± SEM from at least three independent experiments. *$P < 0.05$, **$P < 0.01$, ***$P < 0.001$, ****$P < 0.0001$ indicate significant differences between the indicated groups

whether MSCs could inhibit HSC activation by inducing ferroptosis.

Immunofluorescence analysis showed that in the CCl_4-treated group, both α-SMA and Cox2 expression increased without colocalization, suggesting no ferroptosis in HSCs. However, after MSC treatment, Cox2 expression decreased, and colocalization with α-SMA increased, indicating that MSCs promoted ferroptosis in HSCs, contributing to the reduction of liver fibrosis (Fig. 3A). Following 48 h of treatment with MSCs-CM conditioned medium, Fer-1, and Eras, the viability of mHSCs and LX-2 cells was evaluated via the CCK-8 assay. Results demonstrated that MSCs-CM treatment reduced cell viability, with an additional decline in the MSCs-CM + Eras group. In contrast, cell viability was partially restored in the MSCs-CM + Fer-1 group (Fig. 3B-C). HSCs were co-cultured with MSCs and treated with Fer-1 (Fig. 3D). MSCs significantly reduced the mRNA expression of fibrosis markers α-SMA and TGFB1 in HSCs while increasing the mRNA levels of ferroptosis markers Acsl4 and COX2. Notably, even with the ferroptosis inhibitor Fer-1, MSCs still partially regulated these markers (Fig. 3E-F). At the protein level, MSCs decreased Vimentin, Desmin, α-SMA, TGFB, Sod1, and SOD2 expression in HSCs while enhancing COX2 expression. These effects were partially inhibited by Fer-1 (Fig. 3G-H, Fig. S3A-B). Using DCFH-DA and JC-1 fluorescent probes, MSCs significantly increased ROS generation and decreased mitochondrial membrane potential in HSCs. In contrast, the Fer-1 group showed no significant increase in ROS levels, and mitochondrial membrane potential remained unchanged. In the Fer-1 + MSCs group, although ROS levels were higher than in the Fer-1 group, and mitochondrial membrane potential decreased, the effect was less pronounced than in the MSCs group (Fig. 3I-J). Fe^{2+} and MDA levels were significantly elevated in the MSC-treated group compared to the Control, with Fer-1 partially inhibiting this increase (Fig. 3K-L). MSC-treated HSCs exhibited ferroptosis-related changes, including mitochondrial shrinkage, reduced or absent cristae, and increased electron density (Fig. 3M-N). These findings suggest that MSCs may induce ferroptosis by modulating specific molecular expressions in HSCs, thereby inhibiting their activation.

MSCs induce ferroptosis in HSCs by downregulating GPX4

A total of 83 potential ferroptosis-related genes regulated by MSCs were identified by intersecting 564 ferroptosis-related genes with the 2,395 MSC-regulated genes from our previous RNA-seq analysis (Fig. 4A). Significant gene expression differences between aHSCs and qHSCs were identified through analysis of the GSE229291 dataset (Fig. 4B-C). A comparison of the genes upregulated and downregulated in aHSCs with the 83 ferroptosis-related genes regulated by MSCs suggests that MSCs may regulate 30 upregulated and 22 downregulated ferroptosis-related genes in aHSCs (Fig. 4D, Tab. S6). Notably, the GPX4 gene, significantly upregulated in aHSCs during liver fibrosis, emerged as a gene of particular interest. The analysis of the GSE14323 dataset demonstrated that GPX4 expression levels were markedly elevated in cirrhosis patients relative to healthy individuals ($P = 0.004$), underscoring the critical role of GPX4 in liver fibrosis (Fig. 4E).

The upregulation of Gpx4 expression in CCl_4 and TAA-induced fibrotic mouse models was validated using RNA-seq and immunohistochemistry in subsequent experiments. Gpx4 expression was significantly downregulated by MSC treatment (Fig. 4F-H, Fig. S3C-D). This downregulation was further confirmed by detecting Gpx4 mRNA and protein levels in liver tissue samples (Fig. 4I-J). In vitro experiments also confirmed that MSCs downregulated GPX4 expression in mHSCs and LX-2 cells, even with the ferroptosis inhibitor Fer-1 present, demonstrating a strong regulatory effect (Fig. 4K-L). To further explore GPX4's role in ferroptosis regulation, siRNA was employed to specifically knockdown GPX4. Knockdown of GPX4 in mHSCs and LX-2 cells significantly increased Fe^{2+} and MDA levels, indicating elevated oxidative stress (Fig. 4M-N). In mHSCs, Acsl4 and Cox2 mRNA levels were upregulated, while α-SMA and Tgfb1 were downregulated (Fig. S4A). Similarly, in LX-2 cells, COX2 mRNA levels increased, while α-SMA and TGFB1 levels decreased (Fig. S4B). Gpx4 knockdown increased Cox2 protein levels in mHSCs and concurrently reduced α-SMA, Vimentin, and Sod1 proteins (Fig. 4O, Fig. S4C). In LX-2 cells, α-SMA protein expression decreased, whereas COX2 and ACSL4 proteins increased (Fig. 4P, Fig. S4D). These findings suggest that GPX4 downregulation influences the expression of ferroptosis- and fibrosis-related genes in HSCs, possibly affecting oxidative stress and fibrosis progression.

MSCs promote HSCs ferroptosis via the exosome pathway

In previous research, the effects of MSCs on ferroptosis and HSC activation were investigated using a transwell co-culture system, which eliminated direct cell-to-cell contact. As MSCs primarily exert their effects via exosomes (Exos), this study commenced with exosome extraction and characterization. TEM revealed that Exos displayed a characteristic cup-shaped bilayer membrane structure (Fig. 5A), and NanoFCM analysis indicated an average particle size of 85.2 nm for the extracted Exos (Fig. 5B). Specific markers CD9, and TSG101 were identified in purified exosome samples via Western blot analysis. The endoplasmic reticulum marker Calnexin was detected in MSCs but not in the Exos. These results suggest that the exosome samples were highly purified,

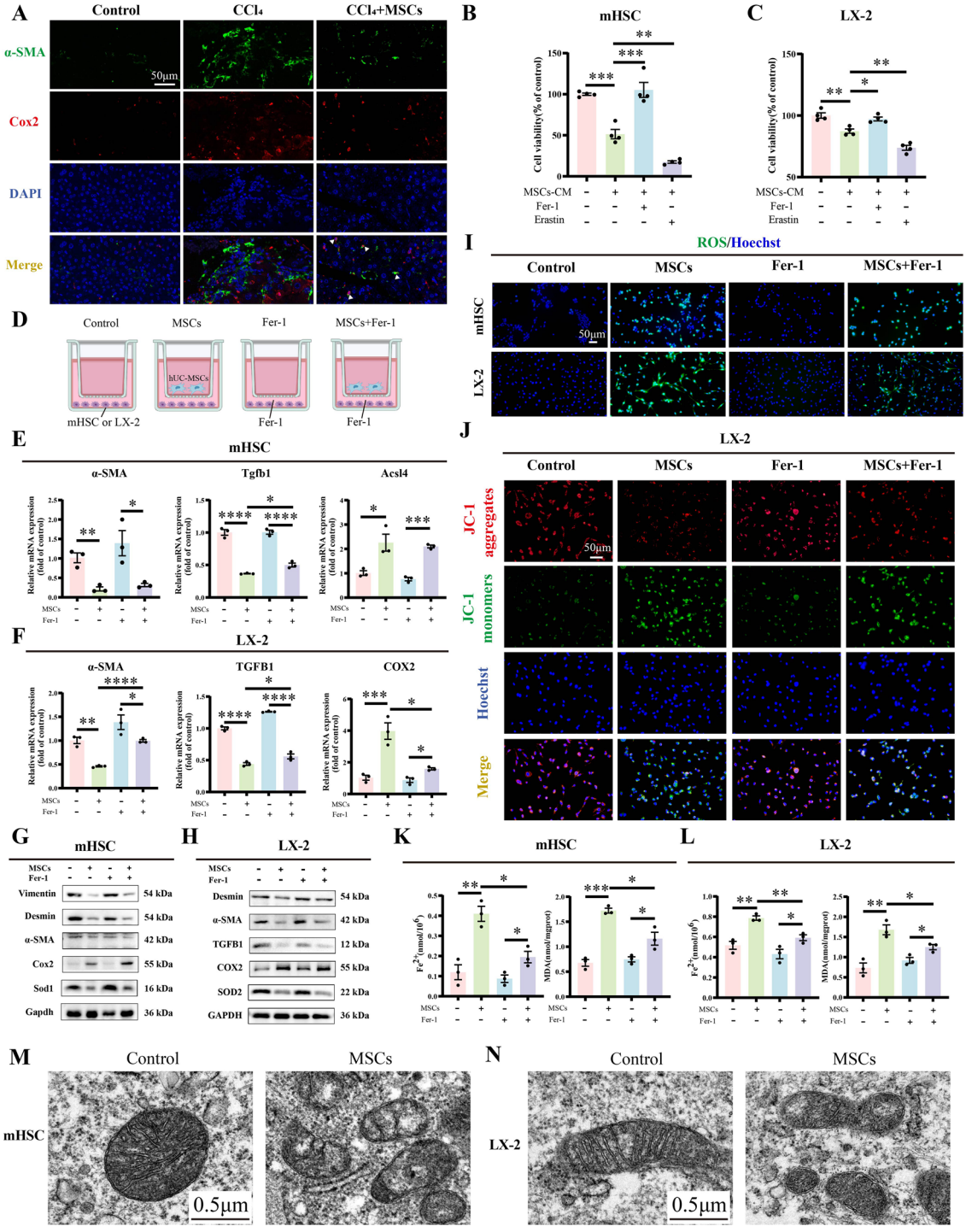

Fig. 3 HSC activation is inhibited by MSCs through the promotion of ferroptosis. (**A**) Immunofluorescence staining of α-SMA (green) and Cox2 (red) in liver tissues. The white triangular region indicates colocalization. Scale bar = 50 μm. (**B**) and (**C**) CCK-8 assays of mHSCs and LX-2 cells viability. (**D**) Schematic of mHSCs and LX-2 cells treated with MSCs and Fer-1 for 48 h. (**E**) qRT-PCR analysis of α-SMA, Tgfb1, and Acsl4 mRNA levels in mHSCs. (**F**) qRT-PCR analysis of α-SMA, TGFB1, and COX2 mRNA levels in LX-2 cells. (**G**) Western blot of Vimentin, Desmin, α-SMA, Cox2, and Sod1 protein levels in mHSCs. (**H**) Western blot of Desmin, α-SMA, TGFB1, COX2, and SOD2 protein levels in LX-2 cells. (**I**) ROS levels in mHSCs and LX-2 cells. Scale bar = 50 μm. (**J**) Mitochondrial membrane potential in LX-2 cells using JC-1 probes. Scale bar = 50 μm. (**K**) and (**L**) Fe^{2+} and MDA levels in mHSCs and LX-2 cells. (**M**) and (**N**) TEM of mitochondrial changes in mHSCs and LX-2 cells. Scale bar = 0.5 μm. The data are presented as the mean ± SEM from at least three independent experiments. *$P < 0.05$, **$P < 0.01$, ***$P < 0.001$, ****$P < 0.0001$ indicate significant differences between the indicated groups

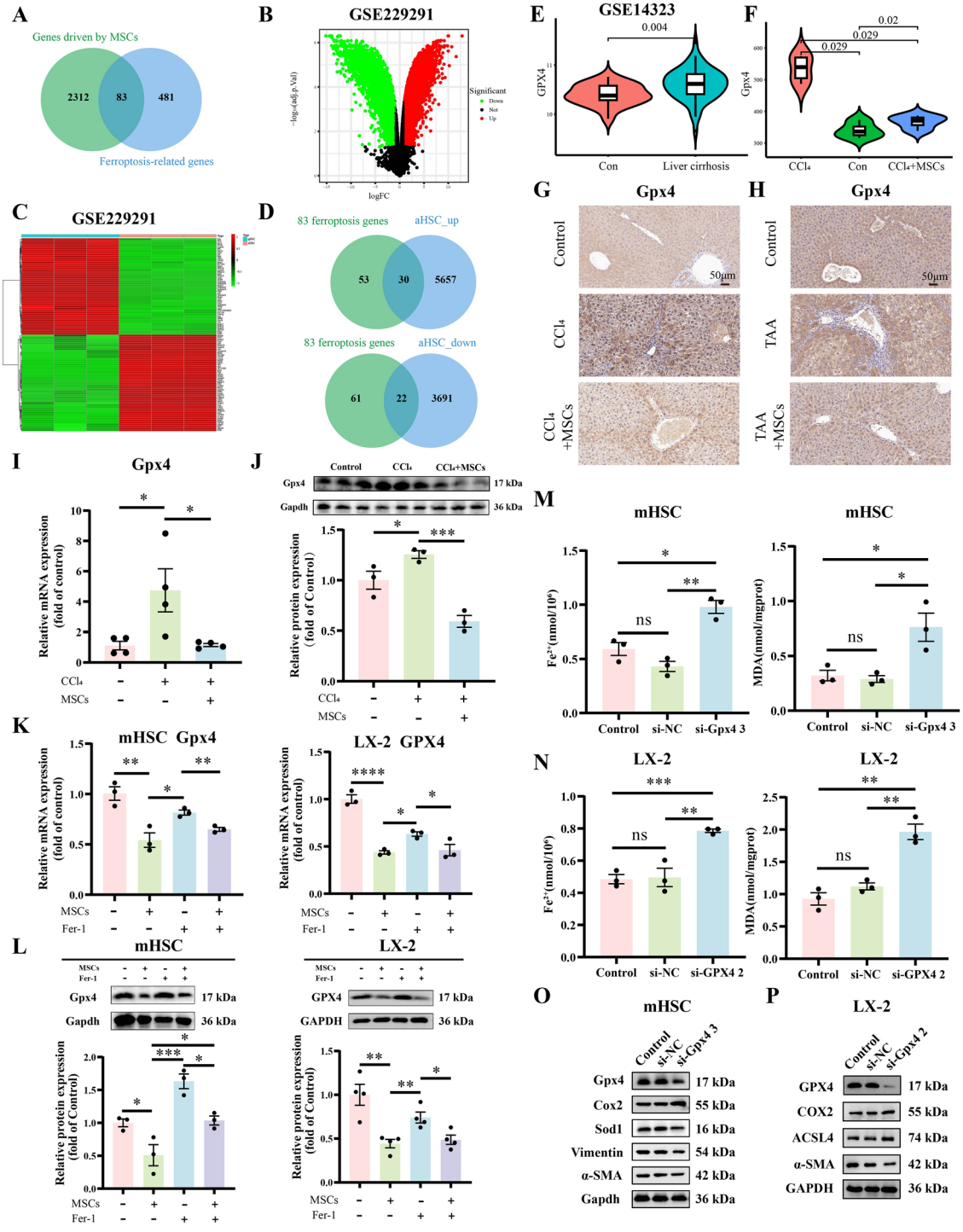

Fig. 4 MSCs suppress HSC activation by promoting ferroptosis through the downregulation of GPX4 in HSCs. (**A**) Ferroptosis-related genes regulated by MSCs. (**B**) and (**C**) Volcano plot and heatmap of DEGs between aHSCs and qHSCs. (**D**) Intersection of 83 ferroptosis genes with up- or down-regulated genes in aHSCs. (**E**) Violin plot showing GPX4 expression in control and cirrhosis patients. (**F**) Violin plot of Gpx4 expression across three sample groups (RNA-seq). (**G**) Immunohistochemistry of Gpx4 expression in Control, CCl_4, and CCl_4 + MSCs groups. Scale bar = 50 μm. (**H**) Immunohistochemistry of Gpx4 expression in Control, TAA, and TAA + MSCs groups. Scale bar = 50 μm. (**I**) qRT-PCR and (**J**) Western Blot analysis of Gpx4 expression in Control, CCl_4, and CCl_4 + MSCs groups. (**K**) qRT-PCR and (**L**) Western Blot analysis of Gpx4 expression in mHSCs and LX-2 cells. (**M**) and (**N**) Fe^{2+} and MDA levels in Control, si-NC, and si-GPX4 groups in mHSCs and LX-2 cells. (**O**) Western Blot images for Gpx4, Cox2, Sod1, Vimentin, and α-SMA in mHSCs. (**P**) Western Blot images for GPX4, COX2, ACSL4, and α-SMA in LX-2 cells. The data are presented as the mean ± SEM from at least three independent experiments. *$P < 0.05$, **$P < 0.01$, ***$P < 0.001$, ****$P < 0.0001$ indicate significant differences between the indicated groups

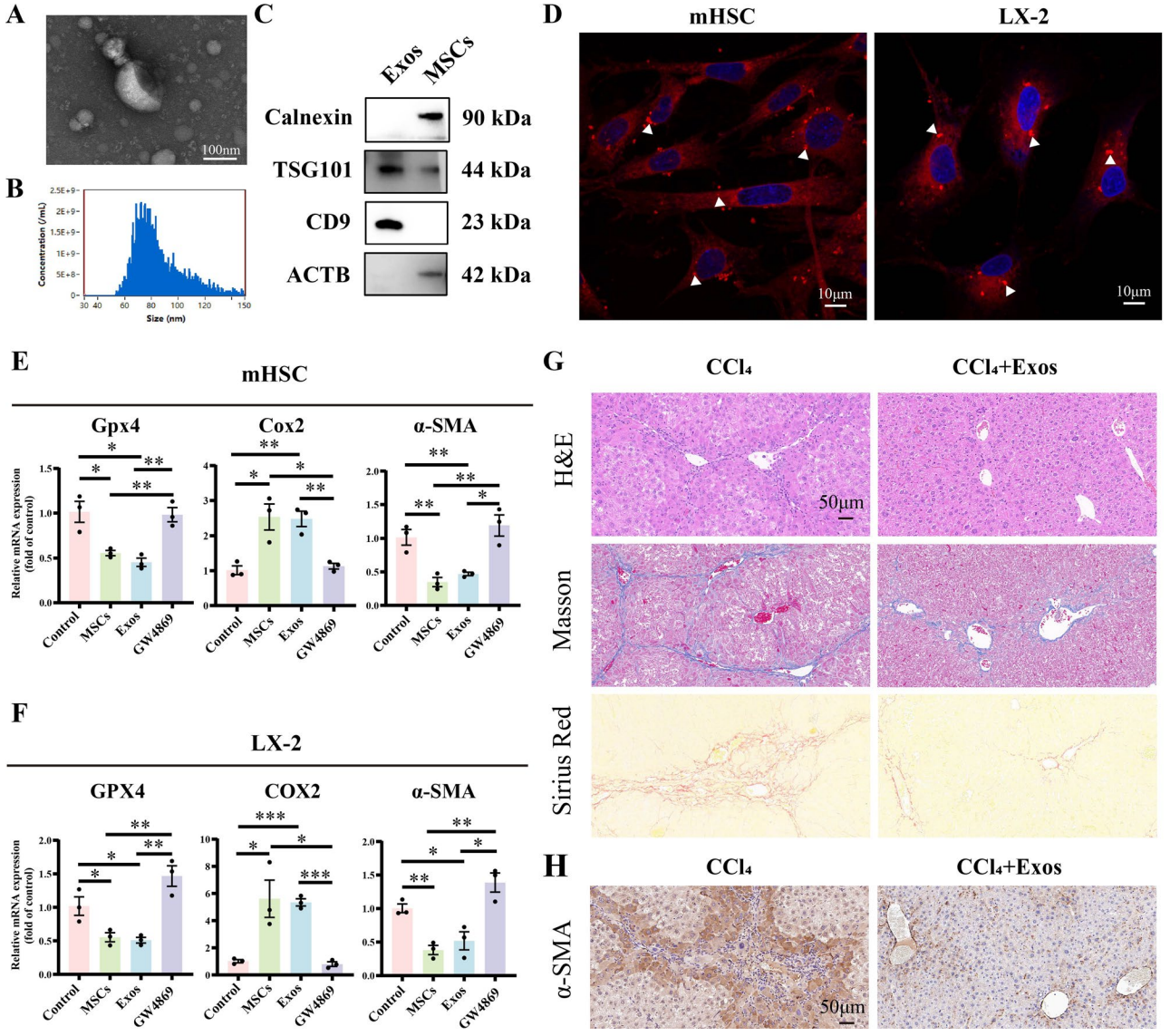

Fig. 5 Ferroptosis in HSCs is induced by MSC-Exos, which alleviates liver fibrosis. (**A**) Exos morphology was determined by TEM. Magnification = 60,000x. Scale bar = 100 nm. (**B**) The particle size of Exos was measured by NanoFCM. (**C**) Exosome-specific markers CD9 and TSG101, along with the endoplasmic reticulum marker Calnexin, were assessed by Western blot. (**D**) The uptake of PKH26-labeled Exos by mHSCs and LX-2 cells was observed using confocal microscopy. The white triangular region indicates exosomes. Scale bar = 10 μm. (**E**) and (**F**) qRT-PCR analysis of GPX4, α-SMA, and COX2 expression in response to Exos treatment, along with the blocking effect of GW4869 pre-treatment on MSCs in mHSCs and LX-2 cells. (**G**) Liver sections from CCl_4 and CCl_4 + Exos groups were stained with H&E, Masson, and Sirius Red. Scale bar = 50 μm. (**H**) Liver sections from CCl_4 and CCl_4 + Exos groups were stained for α-SMA immunohistochemistry. Scale bar = 50 μm. The data are presented as the mean ± SEM from at least three independent experiments. *$P < 0.05$, **$P < 0.01$, ***$P < 0.001$, ****$P < 0.0001$ indicate significant differences between the indicated groups

effectively avoiding contamination from intracellular components (Fig. 5C). The uptake of PKH26-labeled Exos by mHSCs and LX-2 cells was visually confirmed following co-incubation (Fig. 5D).

Further functional studies demonstrated that Exos exhibited effects similar to those of MSCs. Pre-treatment with GW4869 on MSCs inhibited MSC-mediated expression of GPX4, α-SMA, and COX2, confirming the essential role of Exos in inducing HSC ferroptosis and inactivation (Fig. 5E-F). In vivo experiments further validated the therapeutic effects of Exos, showing reduced inflammatory cell infiltration and collagen deposition (Fig. 5G, Fig. S4E). Immunohistochemistry results showed that Exos treatment significantly reduced the elevated α-SMA expression caused by CCl_4(Fig. 5H, Fig. S4F). In summary, these findings provide direct evidence that HSCs undergo ferroptosis and inactivation driven by exosomes secreted by MSCs.

miR-499a-5p in Exos promotes ferroptosis in HSCs by downregulating GPX4

Given that MSC-Exos contain a variety of hsa-miRNAs, mHSCs were chosen instead of LX-2 cells to ensure that the miRNA sequences identified were predominantly those transferred by MSCs, rather than endogenous hsa-miRNAs, which might have been underrepresented. Consequently, miRNA sequencing was conducted under co-culture conditions (Fig. 6A), leading to the identification of two significantly upregulated hsa-miRNAs: hsa-miR-499a-5p and hsa-miR-127-5p (Fig. 6B-C). The target genes of miR-499a-5p and miR-127-5p were predicted using miRDB and TargetScan, followed by functional enrichment analyses to identify miRNAs potentially influencing GPX4 expression via transcriptional regulation. Notably, GPX4 was not among the predicted target genes of either miRNA. GO analysis showed that target genes of miR-499a-5p were significantly enriched in processes such as transcription regulatory region DNA binding and nucleic acid binding (Fig. 6D), directly linked to transcriptional regulation. KEGG pathway analysis further indicated that miR-499a-5p target genes are involved in RNA degradation, cGMP-PKG signaling, and mTOR pathways, all closely associated with transcriptional regulation and cellular metabolism (Fig. 6E). Conversely, miR-127-5p target genes are primarily involved in post-transcriptional regulatory mechanisms, including the ubiquitin ligase complex, cellular protein modification, and ubiquitin-mediated proteolysis (Fig. S5A-B). This suggests that miR-127-5p likely influences protein stability and degradation through post-transcriptional mechanisms, rather than directly regulating transcription. Therefore, given the hidden role of miR-499a-5p in transcriptional regulation and the relevance of its target genes to the GPX4 expression process, we chose miR-499a-5p for further study.

To further validate the transfer and functional relevance of miR-499a-5p, we investigated its enrichment in MSC-Exos and its effect on HSCs. We first confirmed the enrichment of miR-499a-5p in MSC-Exos (Tab. S7). Subsequent analysis revealed that co-culture with MSCs or treatment with MSC-Exos significantly upregulated miR-499a-5p expression in mHSCs and LX-2 cells. However, pre-treatment of MSCs with GW4869 resulted in a marked downregulation of miR-499a-5p expression (Fig. S5C-D). MSC treatment increased the expression of miR-499a-5p in mouse liver tissue (Fig. S5E). These findings revealed that MSCs may deliver miR-499a-5p to fibrotic liver tissue through MSC-Exos. To investigate further the biology of miR-499a-5p, miR-499a-5p mimic was transfected into mHSCs and LX-2 cells (Fig. 6F-G). Following miR-499a-5p upregulation, α-SMA expression decreased, while Acsl4 and Cox2 expression increased in mHSCs (Fig. 6H). Similarly, in LX-2 cells, α-SMA and TGFB1 expression decreased, and ACSL4 and COX2 expression increased (Fig. 6I), aligning with previous findings. GPX4 expression was significantly downregulated in both mHSCs and LX-2 cells following miR-499a-5p mimic transfection (Fig. 6J-K). Post-transfection increases in Fe^{2+} and MDA levels were observed (Fig. 6L-M), along with mitochondrial shrinkage and cristae disappearance, indicating ferroptosis (Fig. 6N-O). These data suggest that miR-499a-5p may downregulate GPX4 expression, inducing ferroptosis in HSCs and inhibiting their activation.

miR-499a-5p targets ETS1 to downregulate GPX4 in Exos-treated HSCs

miR-499a-5p is hypothesized to regulate GPX4 expression at the transcriptional level by targeting transcription factors, based on previous GO and KEGG analyses. To refine the potential target genes of miR-499a-5p, miRDB, TargetScan, and miRTarBase databases were utilized, identifying 11 candidate genes (Fig. 7A). GTRD and human TFBD databases were used to predict transcription factors for human GPX4, while GTRD and animal TFBD databases were employed for mouse Gpx4. By intersecting these predictions with the 11 candidate genes, a common gene, ETS1, was identified in both human and murine datasets (Fig. 7B). No intersecting genes were identified of miR-127-5p, as anticipated (Fig. S5F-G). A Dual-luciferase reporter assay in LX-2 cells was conducted to verify the direct interaction between miR-499a-5p and ETS1. Transfection with miR-499a-5p mimic significantly reduced luciferase activity in the wild-type ETS1 mRNA 3'-UTR group, with no significant change in the mutant group, indicating specific binding (Fig. 7C, Fig. S5H).

Building on our prior research, the interaction between miR-499a-5p and ETS1, along with the potential mechanism involving ETS1 and GPX4, was further investigated. It was initially observed that Exos intervention significantly reduced the mRNA and protein expression of ETS1 and GPX4 in both mHSCs and LX-2 cells (Fig. 7D-G, Fig. S6A). Further experiments demonstrated that transfection with a miR-499a-5p mimic significantly inhibited ETS1 mRNA expression, confirming miR-499a-5p's negative regulatory role on ETS1 (Fig. S6B). Furthermore, after transfection with the miR-499a-5p mimic, Gpx4 and Ets1 protein expression decreased and Acsl4 protein expression increased in mHSCs (Fig. 7H, Fig. S6C), whereas in LX-2 cells, GPX4, ETS1 and SOD1 protein expression decreased and ACSL4 protein expression increased (Fig. 7I, Fig. S6D).

In mouse liver tissues, CCl_4 injection upregulated Ets1 expression, while MSC and MSC-Exos treatment reduced Ets1 mRNA and protein expression (Fig. S6E-F). The regulatory role of ETS1 on GPX4 as a transcription factor

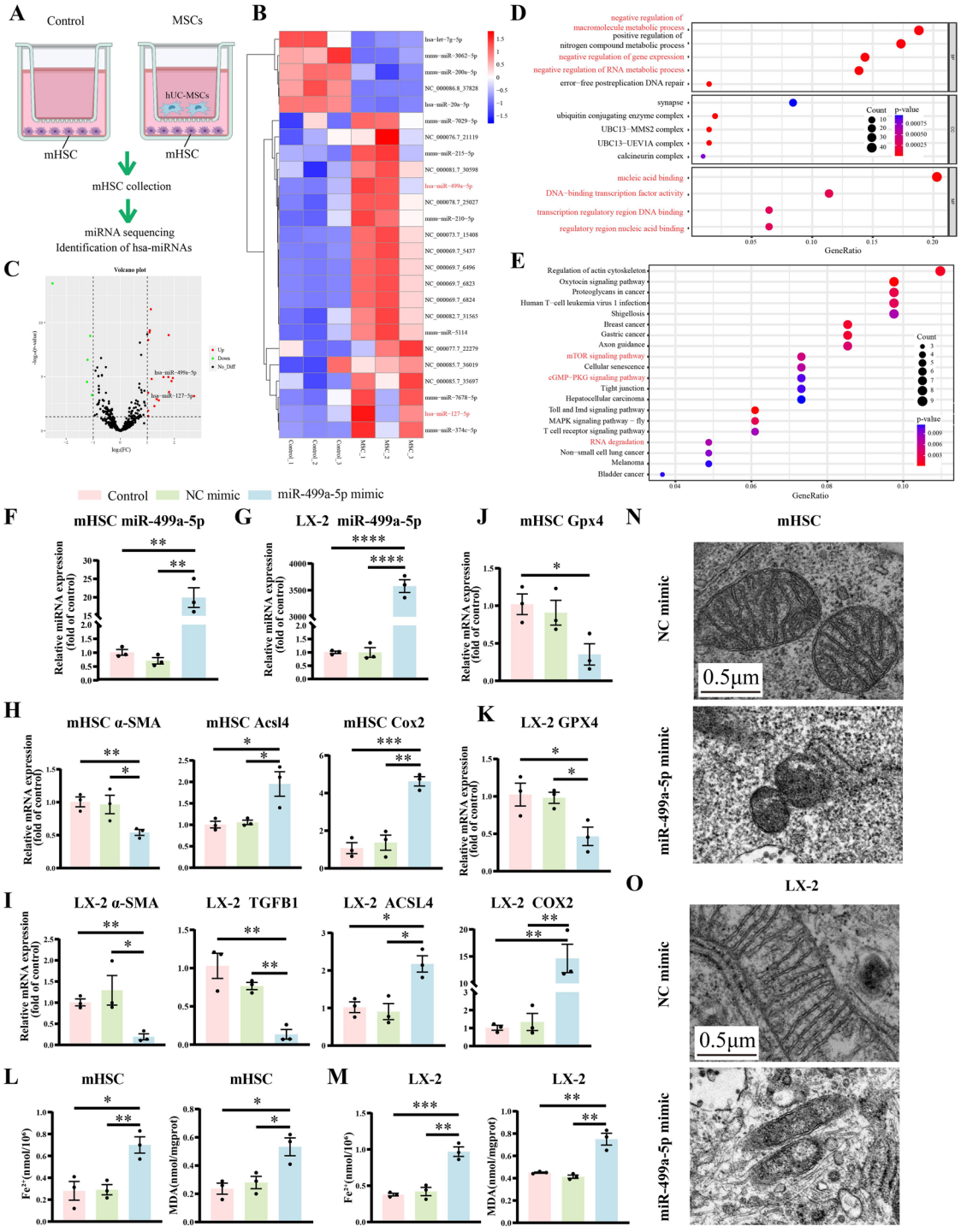

Fig. 6 Ferroptosis in HSCs is promoted by miR-499a-5p through the downregulation of GPX4. (**A**) A schematic diagram illustrating miRNA sequencing preparation. (**B**) and (**C**) Heatmap and volcano plot of miRNA sequencing results. (**D**) GO enrichment analysis for the target genes of miR-499a-5p. (**E**) KEGG enrichment analysis for the target genes of miR-499a-5p. (**F**) and (**G**) Efficiency of miR-499a-5p mimic transfection in mHSCs and LX-2 cells. (**H**) qRT-PCR analysis of α-SMA, Acsl4, and Cox2 in mHSCs transfected with the miR-499a-5p mimic. (**I**) qRT-PCR analysis of α-SMA, TGFB1, ACSL4, and COX2 in LX-2 cells transfected with the miR-499a-5p mimic. (**J**) and (**K**) qRT-PCR analysis of GPX4 in mHSCs and LX-2 cells transfected with the miR-499a-5p mimic. (**L**) and (**M**) Fe^{2+} and MDA levels in mHSCs and LX-2 cells following miR-499a-5p mimic transfection. (**N**) and (**O**) TEM observations of mitochondrial changes in mHSCs and LX-2 cells. Scale bar = 0.5 μm. The data are presented as the mean ± SEM from at least three independent experiments. *$P < 0.05$, **$P < 0.01$, ***$P < 0.001$, ****$P < 0.0001$ indicate significant differences between the indicated groups

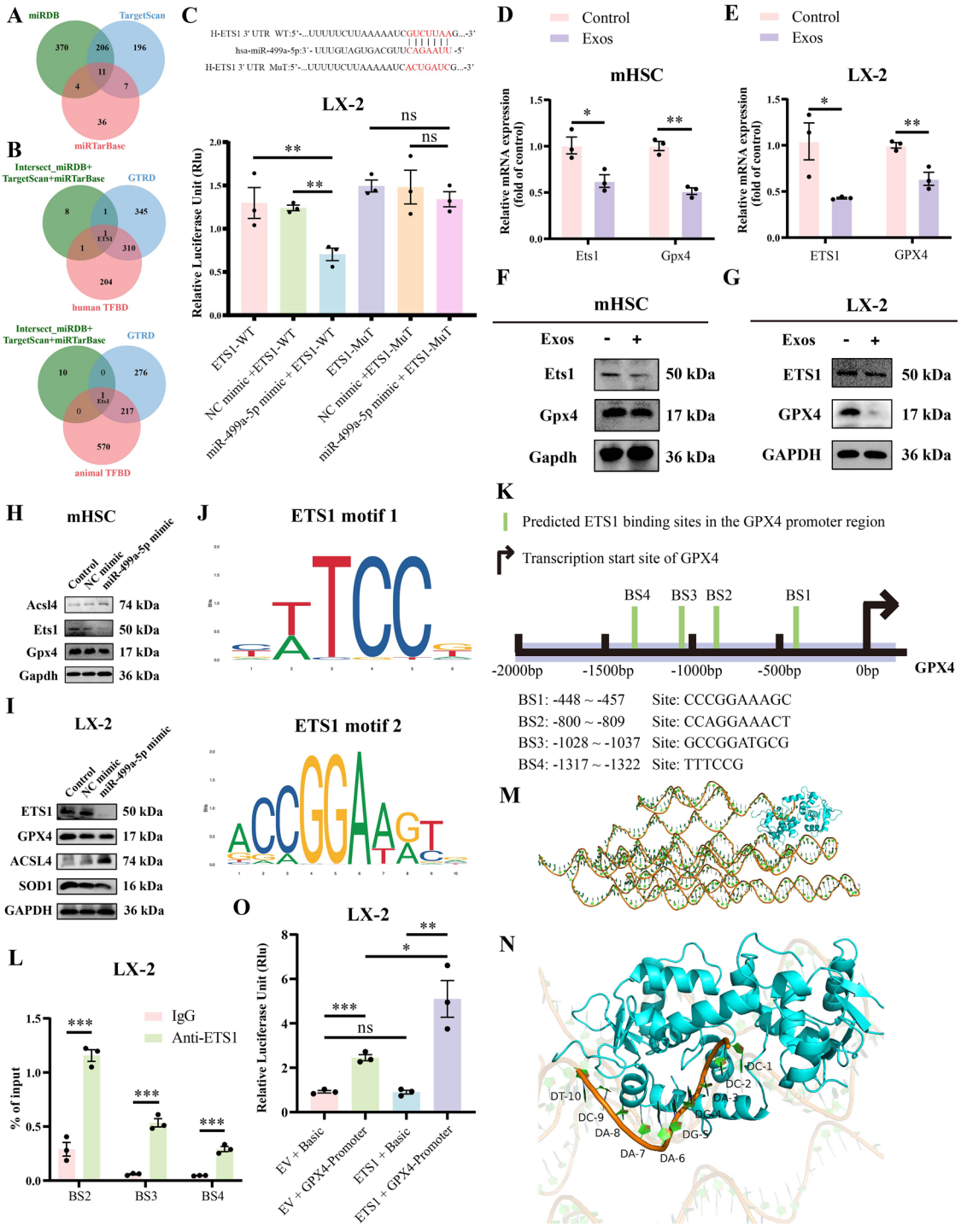

Fig. 7 miR-499a-5p targets ETS1 to downregulate GPX4 in Exos-treated HSCs. (**A**) Venn diagram showing the intersection of miR-499a-5p target genes predicted by miRDB, TargetScan, and miRTarBase databases. (**B**) Venn diagram showing the intersection of 11 target genes with GPX4 transcription factors predicted by GTRD, human TFBD, and animal TFBD databases. (**C**) Dual-luciferase reporter assay of LX-2 cells co-transfected with wild-type or mutant ETS1 mRNA 3′-UTR luciferase plasmids and miR-499a-5p mimic. (**D**) and (**E**) mRNA expression levels of ETS1 and GPX4 in mHSCs and LX-2 cells after Exos intervention. (**F**) and (**G**) Protein expression levels of ETS1 and GPX4 in mHSCs and LX-2 cells after Exos intervention. (**H**) Protein expression levels of Gpx4, Ets1, and Acsl4 in mHSCs after transfection with miR-499a-5p mimic. (**I**) Protein expression levels of ETS1, GPX4, SOD1, and ACSL4 in LX-2 cells after transfection with miR-499a-5p mimic. (**J**) ETS1 motifs were identified using the JASPAR database. (**K**) Schematic representation of potential ETS1 binding sites in the GPX4 promoter. (**L**) ChIP-qPCR analysis confirmed ETS1 binding at BS2, BS3, and BS4 sites on the GPX4 promoter. (**M**) The optimal binding model of the GPX4 promoter DNA sequence with the ETS1 protein is shown in blue. (**N**) ETS1 binds to the GPX4 base sequence CCAGGAAACT (BS2). (**O**) Dual-luciferase reporter assay was conducted to evaluate the transcriptional activity of the GPX4 promoter by ETS1. The data are presented as the mean ± SEM from at least three independent experiments. *$P < 0.05$, **$P < 0.01$, ***$P < 0.001$, ****$P < 0.0001$ indicate significant differences between the indicated groups

was explored by identifying two ETS1 motifs using the JASPAR database (Fig. 7J). Within the 2000 bp upstream region of the GPX4 transcription start site, encompassing the promoter area, four potential binding sites (BS) have been predicted (Fig. 7K). ChIP-qPCR analysis confirmed that BS2, BS3, and BS4 are potential binding sites for ETS1 (Fig. 7L, Fig. S5I). The optimal binding mode between ETS1 and the GPX4 promoter sequence was identified through molecular docking analysis (Fig. 7M). ETS1 interacts with the GPX4 base sequence CCAGGA AACT (BS2) (Fig. 7N). Dual-luciferase reporter assays demonstrated that ETS1 markedly increases the transcriptional regulation of the GPX4 promoter (Fig. 7O, Fig. S6G).

ETS1 knockdown experiments were performed in HSCs to explore the function of ETS1. In mHSCs, Ets1 knockdown resulted in decreased mRNA expression of Gpx4 and Tgfb1, and increased expression of Acsl4 and Cox2 (Fig. S6H). In LX-2 cells, ETS1 knockdown reduced the mRNA expression of GPX4, α-SMA, and TGFB1, while increasing ACSL4 expression, supporting ETS1 as a positive regulator of GPX4 (Fig. S6I). Immunofluorescence analysis of mouse liver tissues revealed that Gpx4 is primarily localized in fibrotic regions, suggesting its potential role in fibrosis. Ets1 was notably detected in the nuclei of cells within these fibrotic areas, implying its function as a transcriptional regulator. MSC and MSC-Exos treatment significantly reduced Ets1 and Gpx4 expression levels (Fig. S7A). Collectively, these data suggest that miR-499a-5p regulates ferroptosis in HSCs by targeting ETS1, leading to downregulation of GPX4 and fibrosis-related genes.

ETS1 overexpression rescues miR-499a-5p-induced ferroptosis

To explore the role of ETS1 in miR-499a-5p-mediated ferroptosis in HSCs, EV and ETS1-overexpressing (OE ETS1) mHSCs and LX-2 cells were established for functional rescue experiments. qRT-PCR and Western blot analyses were performed after transfecting the cells with miR-499a-5p mimic to assess ETS1, GPX4, ACSL4, COX2, and α-SMA expression levels across different groups. In the OE ETS1 group, ETS1, GPX4, and α-SMA mRNA and protein levels were significantly higher than in the EV group, indicating that ETS1 overexpression promotes GPX4 expression and activates HSCs. Further analysis showed that in the OE ETS1 + miR-499a-5p mimic group, ETS1, GPX4, and α-SMA expression levels were significantly higher compared to the EV + miR-499a-5p mimic group, while ACSL4 and COX2 levels were markedly reduced (Fig. 8A-D). Additionally, Fe^{2+} and MDA levels decreased in the OE ETS1 + miR-499a-5p mimic group compared to the EV + miR-499a-5p mimic group (Fig. 8E-F). These findings suggest that ETS1 overexpression can partially counteract miR-499a-5p-mediated ferroptosis, reduce Fe^{2+} and MDA levels, and restore HSCs activity.

To explore the role of ETS1 in liver fibrosis, we analyzed single-cell sequencing data from the Human Protein Atlas (HPA) database. The analysis showed that ETS1 was highly expressed in fibroblasts from human liver tissue (Fig. S7B), suggesting its involvement in liver fibrosis, as activated HSCs acquire fibroblast-like characteristics during the fibrotic response. These findings align with our experimental results, where MSC and MSC-Exos treatments alleviated liver fibrosis by potentially downregulating ETS1. This highlights ETS1 as a critical regulator of ferroptosis in HSCs and a potential therapeutic target for liver fibrosis.

Discussion

The antifibrotic effects of MSCs, achieved primarily by inhibiting HSC activation, are well established and supported by numerous studies [21, 27–29]. Building on these findings, our study delves deeper into the molecular mechanisms underlying these effects, focusing on how hUC-MSCs induce ferroptosis in HSCs via exosomes. Specifically, we identify a novel mechanism by which MSC-exosomes deliver miR-499a-5p to modulate the ETS1/GPX4 pathway, thereby promoting HSC ferroptosis. This mechanism not only reinforces the significant antifibrotic potential of hUC-MSCs but also expands their therapeutic applications in liver fibrosis.

Hepatocytes are the predominant cell type in the liver, and their abundance significantly influences RNA-seq outcomes, particularly in whole-tissue analyses. The enrichment of ferroptosis-related pathways observed in our RNA-seq data reflects the contributions of multiple cell types, with hepatocytes playing a primary role. However, in the pathological context of liver fibrosis and cirrhosis, activated HSCs drive disease progression through excessive extracellular matrix deposition [2, 5, 30]. While RNA-seq data largely capture hepatocyte activity, existing research highlights the therapeutic effects of MSC-Exos through interactions with various liver cell types, rather than targeting a single dominant cell population [31, 32]. Notably, α-SMA and Cox2 co-staining confirms that ferroptosis predominantly occurs in HSCs, underscoring their pivotal role in this process. Given the unique pathological importance of HSCs in fibrosis, targeting MSC-mediated ferroptosis in HSCs represents a promising strategy to mitigate liver fibrosis. Therefore, our study focuses on MSC-Exos-induced ferroptosis in HSCs to explore its therapeutic potential in fibrosis treatment.

Prior research on MSCs has primarily focused on apoptosis, inactivation, and Epithelial-Mesenchymal Transition (EMT), with limited studies on ferroptosis

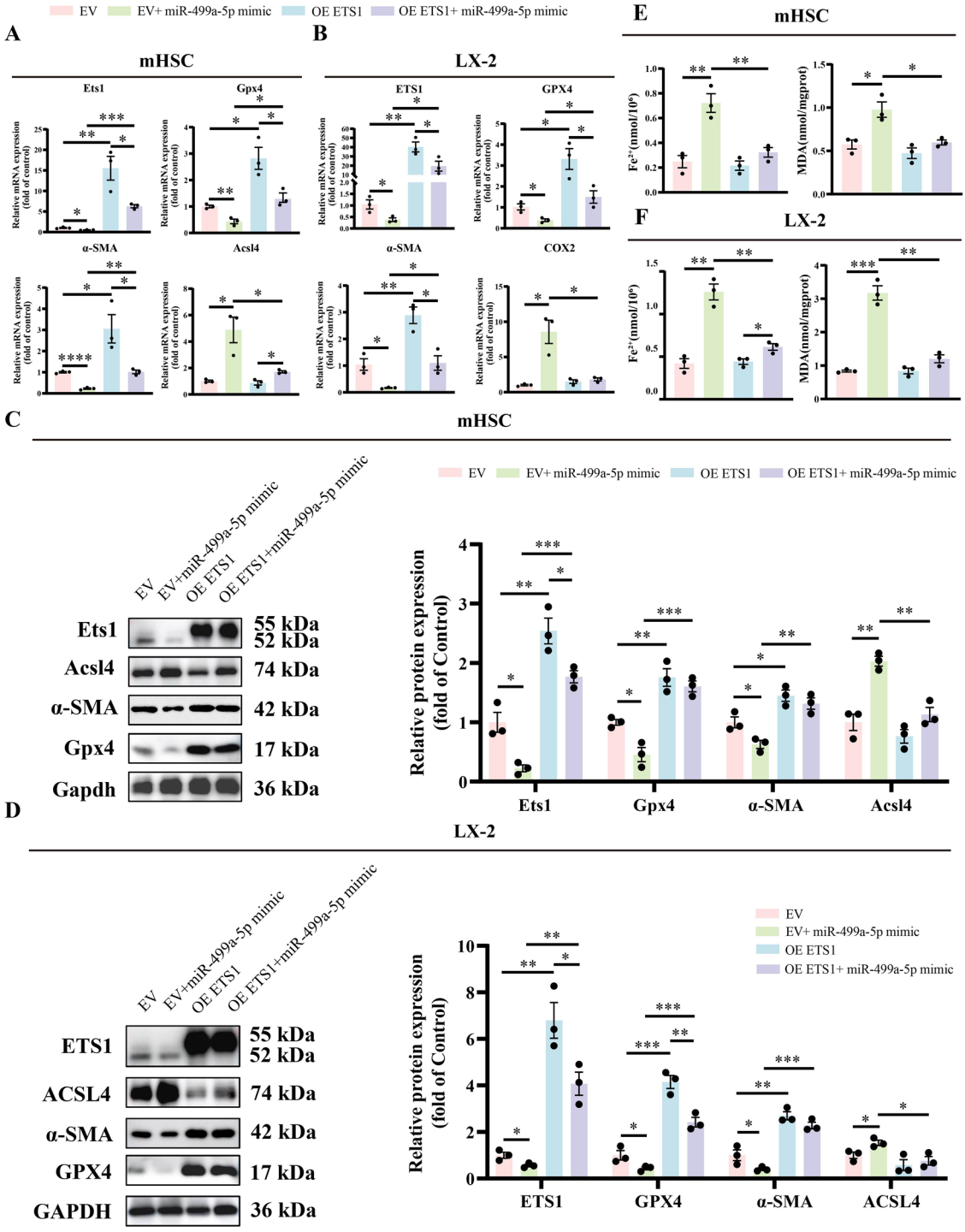

Fig. 8 ETS1 overexpression rescues cells from miR-499a-5p-induced ferroptosis. (**A**) mRNA levels of Ets1, Gpx4, α-SMA, and Acsl4 in mHSCs after Ets1 overexpression and miR-499a-5p mimic transfection. (**B**) mRNA levels of ETS1, GPX4, α-SMA, and COX2 in LX-2 cells after ETS1 overexpression and miR-499a-5p mimic transfection. (**C**) and (**D**) Protein levels of ETS1, GPX4, α-SMA, and ACSL4 in mHSCs and LX-2 cells after ETS1 overexpression and miR-499a-5p mimic transfection. (**E**) and (**F**) Fe^{2+} and MDA levels in mHSCs and LX-2 cells after ETS1 overexpression and miR-499a-5p mimic transfection. The data are presented as the mean ± SEM from at least three independent experiments. *$P < 0.05$, **$P < 0.01$, ***$P < 0.001$, ****$P < 0.0001$ indicate significant differences between the indicated groups

regulation in HSCs [15, 21, 29, 33]. Recent studies indicate that regulating ferroptosis in HSCs significantly influences liver fibrosis progression [34–36]. For example, Celastrol alleviates fibrosis by inducing HSC ferroptosis via PRDX targeting and HO-1 upregulation [37]. Our findings advance this field by demonstrating that hUC-MSCs regulate GPX4-mediated ferroptosis in HSCs via miR-499a-5p, a previously unexplored mechanism.

It is important to emphasize that, although our study shows that hUC-MSCs inhibit HSC activation by inducing ferroptosis, they also exhibit an inhibitory effect on ferroptosis at the tissue level in the liver. This duality may result from the selective delivery of exosomal cargo. For instance, MSC-Exos deliver miR-26a and BECN1 to HSCs, enhancing ferroptosis [38, 39], while delivering miR-204-5p and miR-124-3p to hepatocytes, promoting antioxidant pathways and protecting against ferroptosis [40, 41]. Additionally, the liver injury microenvironment influences exosome uptake, enabling MSCs to selectively regulate key cells [16]. These findings highlight the selectivity and adaptability of MSC-Exos in modulating the fibrotic microenvironment.

The interaction between hUC-MSCs and HSCs via a transwell system suggests that hUC-MSCs exert their effects through indirect rather than direct contact. Having established the role of ferroptosis in HSC regulation, we next explored the molecular vehicles through which hUC-MSCs exert these effects, focusing on exosomes and their miRNA cargo. Exosomes are extracellular vesicles that carry bioactive molecules such as lipids, proteins, and nucleic acids, including DNA, RNA, and microRNAs Exosomes are extracellular vesicles that encapsulate bioactive substances, including proteins, lipids, and genetic material such as DNA, RNA, and microRNAs [42, 43]. As key components of exosomes, miRNAs are essential in regulating gene expression and mediating cell-to-cell communication [44–46]. For example, Song et al. showed that MSC-Exos could inhibit DMT1 expression via miR-23a-3p, leading to the suppression of ferroptosis and alleviation of myocardial injury [47]. In this study, we found that miR-499a-5p is transferred to HSCs via MSC-Exos and mediates ferroptosis in HSCs by targeting ETS1. Notably, the expression of miR-499a-5p is decreased in hepatitis B-associated liver fibrosis patient and linked to chronic inflammation, supporting the idea that MSC-Exos delivering miR-499a-5p may alleviate liver fibrosis [48].

By binding to promoter DNA, transcription factors regulate gene expression, which is essential for cell growth, differentiation, and differentiation [49]. ETS proto-oncogene 1 (ETS1), a key transcription factor in the ETS family, possesses a conserved DNA-binding domain that recognizes and binds to the GGAA/T core sequence of target genes, significantly contributing to tumor invasion, metastasis, and fibrosis [50–52]. The liver expresses ETS1 primarily in HSCs and endothelial cells, where it plays a role in activating HSCs and promoting fibrosis via TGFβ-Smad2/3 pathway [53]. Our results show that ETS1 expression is significantly elevated in fibrotic liver tissues and is effectively downregulated by MSC treatment. Previous studies demonstrate that ADSC-CM reduces myocardial fibrosis and apoptosis by delivering miR-221/222, which downregulates ETS1 and PUMA expression [54]. Particulate matter induces pulmonary fibrosis by upregulating ETS1 and promoting EMT [55]. Additionally, ETS1 induces hepatocyte apoptosis through the TGF-β1/Smad3 pathway, promoting liver inflammation and fibrosis in a NASH mouse model [56]. However, ETS1's specific role in HSC ferroptosis remains insufficiently explored. Our study found that MSC-Exos intervention significantly downregulated ETS1 and its downstream target GPX4 in HSCs. Transfection with miR-499a-5p mimics and ETS1 knockdown both upregulated HSC ferroptosis markers and downregulated fibrosis markers. Conversely, ETS1 overexpression restored HSC resistance to ferroptosis. These findings clarify ETS1's regulatory role in HSC ferroptosis and suggest it as a potential target in the treatment of liver fibrosis.

In this study, the use of a universal primer to detect miR-499a-5p complicates the distinction between MSC-derived exosomal miR-499a-5p and endogenous miR-499a-5p, as both share identical mature sequences. Despite this limitation, we observed a significant increase in miR-499a-5p levels in mHSCs and LX-2 cells after co-culturing with MSCs or MSC-Exos, suggesting that exosomes are likely the main source. The increase in miR-499a-5p was closely associated with MSC exosomes, supporting the hypothesis of exosomal delivery. However, we cannot completely rule out the possibility of endogenous miR-499a-5p expression, especially as other bioactive molecules in exosomes may influence its expression.

Overall, this study offers fresh perspectives on the induction of ferroptosis in HSCs and the improvement of liver fibrosis by hUC-MSCs via the regulation of the ETS1/GPX4 pathway through MSC-Exos. These findings underscore the need for further research into how hUC-MSCs regulate ferroptosis across different microenvironments and whether this regulation depends on specific signaling pathways or intercellular interactions. Techniques such as single-cell RNA sequencing, proteomics, and miRNA analyses will help uncover the underlying mechanisms of MSC-exosome selectivity and optimize their therapeutic potential in chronic liver diseases. The discovery of this mechanism suggests new strategies for liver fibrosis treatment and establishes the foundation for the broader application of MSC-Exos. Future research should optimize MSC-Exos application strategies and

further validate their clinical efficacy to provide more effective treatment options for liver fibrosis.

Abbreviations

ALT	Alanine aminotransferase
AST	Aspartate aminotransferase
ALP	Alkaline phosphatase
ALB	Albumin
CCl_4	Carbon tetrachloride
ECM	Excessive extracellular matrix
ETS1	Transcription factor E26 transformation-specific 1
Eras	Erastin;
Fer-1	Ferrostatin-1
GSH	Glutathione
GPX4	Glutathione peroxidase 4
HSCs	Hepatic stellate cells
aHSCs	Activated hepatic stellate cells
qHSCs	Quiescent hepatic stellate cells
hUC-MSCs	Human umbilical cord-derived mesenchymal stem cells
MSC-Exos	MSC-derived exosomes
MSCs-CM	MSCs conditioned medium
IL-6	Interleukin-6
IL-10	Interleukin-10
IL-1β	Interleukin-1β
MDA	Malondialdehyde
MSCs	Mesenchymal stem cells
TAA	Thioacetamide
TNF-α	Tumor necrosis factor-α
TEM	Transmission electron microscopy
ROS	Reactive oxygen species

Supplementary Information

The online version contains supplementary material available at https://doi.org/10.1186/s12951-025-03291-4.

Supplementary Material 1

Supplementary Material 2

Supplementary Material 3

Supplementary Material 4

Acknowledgements

We extend our gratitude to Shenzhen Wingor Biological Co., Ltd. for supplying the hUC-MSCs. We also appreciate the GEO, JASPAR, HPA, UniProt, PDBe, GTRD, TFBD, TargetScan, miRDB, and miRTarBase databases for generously sharing extensive datasets. We regret any unintentional omissions of citations and references due to space constraints.

Author contributions

YAJ and YCX conceptualized and supervised the overall project. ZW and MQY performed the cell culture experiments and contributed to the initial manuscript draft. LCY conducted statistical analysis, while ZYX handled data visualization and interpretation. ZW also managed figure production, and MQY carried out bioinformatics analysis. KD and PJL performed histological assessments, PC and MHS were responsible for in vivo data collection, and KS coordinated the animal treatments. YAJ and YCX critically revised the manuscript. All authors reviewed and approved the final version.

Funding

This work was supported by the National Natural Science Foundation of China (No. 81972673), the Anti-aging Research Center of Wuhan University Education Development Foundation (No. 2002330), the Fundamental Research Funds for the Central Universities (project no. 2042024kf0026) and the National Stem Cell Clinical Research Project of China.

Data availability

No datasets were generated or analysed during the current study.

Declarations

Ethical approval

The animal study adhered to the guidelines set forth by the Declaration of Helsinki, and the research protocol received approval from the Animal Care and Use Committee at Renmin Hospital of Wuhan University (Approval Nos. 20220901 A, 20230103 C).

Consent for publication

Not applicable.

Competing interests

The authors declare no competing interests.

Author details

[1]Department of Infectious Diseases, Renmin Hospital of Wuhan University, Wuhan, China
[2]Department of Ultrasound Medicine, Union Hospital, Tongji Medical College, Huazhong University of Science and Technology, Wuhan, China
[3]State Key Laboratory of Virology and Hubei Province Key Laboratory of Allergy and Immunology, Institute of Medical Virology, TaiKang Center for Life and Medical Sciences, TaiKang Medical School, Wuhan University, Wuhan, China
[4]Hubei Jiangxia Laboratory, Wuhan, China
[5]Pingyuan Laboratory, Henan, China

Received: 1 October 2024 / Accepted: 3 March 2025
Published online: 19 March 2025

References

1. Horn P, Tacke F. Metabolic reprogramming in liver fibrosis. Cell Metab. 2024;36:1439–55. https://doi.org/10.1016/j.cmet.2024.05.003.
2. Hammerich L, Tacke F. Hepatic inflammatory responses in liver fibrosis. Nat Rev Gastroenterol Hepatol. 2023;20:633–46. https://doi.org/10.1038/s41575-023-00807-x.
3. Tsuchida T, Friedman SL. Mechanisms of hepatic stellate cell activation. Nat Rev Gastroenterol Hepatol. 2017;14:397–411. https://doi.org/10.1038/nrgastro.2017.38.
4. Iredale JP. Models of liver fibrosis: exploring the dynamic nature of inflammation and repair in a solid organ. J Clin Invest. 2007;117:539–48. https://doi.org/10.1172/jci30542.
5. Kisseleva T, Brenner D. Molecular and cellular mechanisms of liver fibrosis and its regression. Nat Rev Gastroenterol Hepatol. 2021;18:151–66. https://doi.org/10.1038/s41575-020-00372-7.
6. Dixon SJ, Olzmann JA. The cell biology of ferroptosis. Nat Rev Mol Cell Biol. 2024;25:424–42. https://doi.org/10.1038/s41580-024-00703-5.
7. Chen J, Li X, Ge C, Min J, Wang F. The multifaceted role of ferroptosis in liver disease. Cell Death Differ. 2022;29:467–80. https://doi.org/10.1038/s41418-022-00941-0.
8. Chen X, Li J, Kang R, Klionsky DJ, Tang D. Ferroptosis: machinery and regulation. Autophagy. 2021;17:2054–81. https://doi.org/10.1080/15548627.2020.1810918.
9. Yamada N, Karasawa T, Kimura H, Watanabe S, Komada T, Kamata R, Sampilvanjil A, Ito J, Nakagawa K, Kuwata H, et al. Ferroptosis driven by radical oxidation of n-6 polyunsaturated fatty acids mediates acetaminophen-induced acute liver failure. Cell Death Dis. 2020;11:144. https://doi.org/10.1038/s41419-020-2334-2.
10. Yu Y, Jiang L, Wang H, Shen Z, Cheng Q, Zhang P, Wang J, Wu Q, Fang X, Duan L, et al. Hepatic transferrin plays a role in systemic iron homeostasis and liver ferroptosis. Blood. 2020;136:726–39. https://doi.org/10.1182/blood.2019002907.
11. Huang S, Wang Y, Xie S, Lai Y, Mo C, Zeng T, Kuang S, Zhou C, Zeng Z, Chen Y, et al. Isoliquiritigenin alleviates liver fibrosis through caveolin-1-mediated hepatic stellate cells ferroptosis in zebrafish and mice. Phytomedicine. 2022;101:154117. https://doi.org/10.1016/j.phymed.2022.154117.
12. Xu S, Chen Y, Miao J, Li Y, Liu J, Zhang J, Liang J, Chen S, Hou S. Esculin inhibits hepatic stellate cell activation and CCl(4)-induced liver fibrosis by activating the Nrf2/GPX4 signaling pathway. Phytomedicine. 2024;128:155465. https://doi.org/10.1016/j.phymed.2024.155465.

13. Yuan S, Wei C, Liu G, Zhang L, Li J, Li L, Cai S, Fang L. Sorafenib attenuates liver fibrosis by triggering hepatic stellate cell ferroptosis via HIF-1α/SLC7A11 pathway. Cell Prolif. 2022;55:e13158. https://doi.org/10.1111/cpr.13158.
14. Tian S, Zhou X, Zhang M, Cui L, Li B, Liu Y, Su R, Sun K, Hu Y, Yang F, et al. Mesenchymal stem cell-derived exosomes protect against liver fibrosis via delivering miR-148a to target KLF6/STAT3 pathway in macrophages. Stem Cell Res Ther. 2022;13. https://doi.org/10.1186/s13287-022-03010-y.
15. Zhang Z, Shang J, Yang Q, Dai Z, Liang Y, Lai C, Feng T, Zhong D, Zou H, Sun L, et al. Exosomes derived from human adipose mesenchymal stem cells ameliorate hepatic fibrosis by inhibiting PI3K/Akt/mTOR pathway and remodeling choline metabolism. J Nanobiotechnol. 2023;21. https://doi.org/10.1186/s12951-023-01788-4.
16. Caplan AI, Correa D. The MSC: an injury drugstore. Cell Stem Cell. 2011;9:11–5. https://doi.org/10.1016/j.stem.2011.06.008.
17. Yao S, Pang M, Wang Y, Wang X, Lin Y, Lv Y, Xie Z, Hou J, Du C, Qiu Y, et al. Mesenchymal stem cell attenuates spinal cord injury by inhibiting mitochondrial quality control-associated neuronal ferroptosis. Redox Biol. 2023;67. https://doi.org/10.1016/j.redox.2023.102871.
18. Lin F, Chen W, Zhou J, Zhu J, Yao Q, Feng B, Feng X, Shi X, Pan Q, Yu J, et al. Mesenchymal stem cells protect against ferroptosis via exosome-mediated stabilization of SLC7A11 in acute liver injury. Cell Death Dis. 2022;13:271. https://doi.org/10.1038/s41419-022-04708-w.
19. Manuelpillai U, Lourensz D, Vaghjiani V, Tchongue J, Lacey D, Tee JY, Murthi P, Chan J, Hodge A, Sievert W. Human amniotic epithelial cell transplantation induces markers of alternative macrophage activation and reduces established hepatic fibrosis. PLoS ONE. 2012;7:e38631. https://doi.org/10.1371/journal.pone.0038631.
20. Zhang XW, Zhou JC, Peng D, Hua F, Li K, Yu JJ, Lv XX, Cui B, Liu SS, Yu JM, et al. Disrupting the TRIB3-SQSTM1 interaction reduces liver fibrosis by restoring autophagy and suppressing exosome-mediated HSC activation. Autophagy. 2020;16:782–96. https://doi.org/10.1080/15548627.2019.1635383.
21. Cheng F, Yang F, Wang Y, Zhou J, Qian H, Yan Y. Mesenchymal stem cell-derived Exosomal miR-27b-3p alleviates liver fibrosis via downregulating YAP/LOXL2 pathway. J Nanobiotechnol. 2023;21:195. https://doi.org/10.1186/s12951-023-01942-y.
22. Hong S, Lee DS, Bae GW, Jeon J, Kim HK, Rhee S, Jung KO. In vivo stem cell imaging principles and applications. Int J Stem Cells. 2023;16:363–75. https://doi.org/10.15283/ijsc23045.
23. Sun Y, Liu Q, Qin Y, Xu Y, Zhao J, Xie Y, Li C, Qin T, Jin Y, Jiang L, et al. Exosomes derived from CD271(+)CD56(+) bone marrow mesenchymal stem cell subpopoulation identified by single-cell RNA sequencing promote axon regeneration after spinal cord injury. Theranostics. 2024;14:510–27. https://doi.org/10.7150/thno.89008.
24. Zhang Y, Zhang Y, Chen T, Lin Y, Gong J, Xu Q, Wang J, Li J, Meng Y, Li Y, et al. Caveolin-1 depletion attenuates hepatic fibrosis via promoting SQSTM1-mediated PFKL degradation in HSCs. Free Radic Biol Med. 2023;204:95–107. https://doi.org/10.1016/j.freeradbiomed.2023.04.009.
25. Mas VR, Maluf DG, Archer KJ, Yanek K, Kong X, Kulik L, Freise CE, Olthoff KM, Ghobrial RM, McIver P, et al. Genes involved in viral carcinogenesis and tumor initiation in hepatitis C virus-induced hepatocellular carcinoma. Mol Med. 2009;15:85–94. https://doi.org/10.2119/molmed.2008.00110.
26. Zhou N, Yuan X, Du Q, Zhang Z, Shi X, Bao J, Ning Y, Peng L. FerrDb V2: update of the manually curated database of ferroptosis regulators and ferroptosis-disease associations. Nucleic Acids Res. 2023;51:D571–82. https://doi.org/10.1093/nar/gkac935.
27. Lu X, Guo H, Wei X, Lu D, Shu W, Song Y, Qiu N, Xu X. Current status and prospect of delivery vehicle based on mesenchymal stem Cell-Derived exosomes in liver diseases. Int J Nanomed. 2023;18:2873–90. https://doi.org/10.2147/ijn.S404925.
28. Yuan M, Yao L, Chen P, Wang Z, Liu P, Xiong Z, Hu X, Li L, Jiang Y. Human umbilical cord mesenchymal stem cells inhibit liver fibrosis via the microRNA-148a-5p/SLIT3 axis. Int Immunopharmacol. 2023;125:111134. https://doi.org/10.1016/j.intimp.2023.111134.
29. Zheng W, Bian S, Qiu S, Bishop CE, Wan M, Xu N, Sun X, Sequeira RC, Atala A, Gu Z, et al. Placenta mesenchymal stem cell-derived extracellular vesicles alleviate liver fibrosis by inactivating hepatic stellate cells through a miR-378c/SKP2 axis. Inflamm Regen. 2023;43. https://doi.org/10.1186/s41232-023-00297-z.
30. Zhang D, Zhang Y, Sun B. The molecular mechanisms of liver fibrosis and its potential therapy in application. Int J Mol Sci. 2022;23. https://doi.org/10.3390/ijms232012572.
31. Zhu M, Hua T, Ouyang T, Qian H, Yu B. Applications of Mesenchymal Stem Cells in Liver Fibrosis: Novel Strategies, Mechanisms, and Clinical Practice. *Stem Cells Int* 2021, *2021*, 6546780. https://doi.org/10.1155/2021/6546780
32. Hazrati A, Malekpour K, Soudi S, Hashemi SM. Mesenchymal stromal/stem cells and their extracellular vesicles application in acute and chronic inflammatory liver diseases: emphasizing on the Anti-Fibrotic and Immunomodulatory mechanisms. Front Immunol. 2022;13:865888. https://doi.org/10.3389/fimmu.2022.865888.
33. Huang T, Zhang C, Shang Z, Shuai Q, Nie L, Ren J, Hou S, Xie J. Bone mesenchymal stem cells improve cholestatic liver fibrosis by targeting ULK1 to regulate autophagy through PI3K/AKT/mTOR pathway. Stem Cells Transl Med. 2024;13:648–60. https://doi.org/10.1093/stcltm/szae028.
34. Deng Y, Lu L, Zhu D, Zhang H, Fu Y, Tan Y, Tan X, Guo M, Zhang Y, Yang H, et al. MafG/MYH9-LCN2 axis promotes liver fibrosis through inhibiting ferroptosis of hepatic stellate cells. Cell Death Differ. 2024. https://doi.org/10.1038/s41418-024-01322-5.
35. Lang Z, Yu S, Hu Y, Tao Q, Zhang J, Wang H, Zheng L, Yu Z, Zheng J. Ginsenoside Rh2 promotes hepatic stellate cell ferroptosis and inactivation via regulation of IRF1-inhibited SLC7A11. *Phytomedicine* 2023, *118*, 154950. https://doi.org/10.1016/j.phymed.2023.154950
36. Kitsugi K, Noritake H, Matsumoto M, Hanaoka T, Umemura M, Yamashita M, Takatori S, Ito J, Ohta K, Chida T, et al. Simvastatin inhibits hepatic stellate cells activation by regulating the ferroptosis signaling pathway. Biochim Biophys Acta Mol Basis Dis. 2023;1869:166750. https://doi.org/10.1016/j.bbadis.2023.166750.
37. Luo P, Liu D, Zhang Q, Yang F, Wong YK, Xia F, Zhang J, Chen J, Tian Y, Yang C, et al. Celastrol induces ferroptosis in activated HSCs to ameliorate hepatic fibrosis via targeting Peroxiredoxins and HO-1. Acta Pharm Sin B. 2022;12:2300–14. https://doi.org/10.1016/j.apsb.2021.12.007.
38. Cao Y, Yang H, Huang Y, Lu J, Du H, Wang B. Mesenchymal stem cell-derived Exosomal miR-26a induces ferroptosis, suppresses hepatic stellate cell activation, and ameliorates liver fibrosis by modulating SLC7A11. Open Med (Wars). 2024;19:20240945. https://doi.org/10.1515/med-2024-0945.
39. Tan Y, Huang Y, Mei R, Mao F, Yang D, Liu J, Xu W, Qian H, Yan Y. HucMSC-derived exosomes delivered BECN1 induces ferroptosis of hepatic stellate cells via regulating the xCT/GPX4 axis. Cell Death Dis. 2022;13:319. https://doi.org/10.1038/s41419-022-04764-2.
40. Tian X, Wu L, Li X, Zheng W, Zuo H, Song H. Exosomes derived from bone marrow mesenchymal stem cells alleviate biliary ischemia reperfusion injury in fatty liver transplantation by inhibiting ferroptosis. Mol Cell Biochem. 2024;479:881–94. https://doi.org/10.1007/s11010-023-04770-8.
41. Wu L, Tian X, Zuo H, Zheng W, Li X, Yuan M, Tian X, Song H. miR-124-3p delivered by exosomes from Heme oxygenase-1 modified bone marrow mesenchymal stem cells inhibits ferroptosis to attenuate ischemia-reperfusion injury in steatotic grafts. J Nanobiotechnol. 2022;20:196. https://doi.org/10.1186/s12951-022-01407-8.
42. Lin Z, Wu Y, Xu Y, Li G, Li Z, Liu T. Mesenchymal stem cell-derived exosomes in cancer therapy resistance: recent advances and therapeutic potential. Mol Cancer. 2022;21:179. https://doi.org/10.1186/s12943-022-01650-5.
43. Cunha ERK, Ying W, Olefsky JM. Exosome-Mediated impact on systemic metabolism. Annu Rev Physiol. 2024;86:225–53. https://doi.org/10.1146/annurev-physiol-042222-024535.
44. Hong T, Zhao T, He W, Xia J, Huang Q, Yang J, Gu W, Chen C, Zhang N, Liu Y, et al. Exosomal circBBS2 inhibits ferroptosis by targeting miR-494 to activate SLC7A11 signaling in ischemic stroke. Faseb J. 2023;37:e23152. https://doi.org/10.1096/fj.202300317RRR.
45. Kong R, Ji L, Pang Y, Zhao D, Gao J. Exosomes from Osteoarthritic fibroblast-like synoviocytes promote cartilage ferroptosis and damage via delivering microRNA-19b-3p to target SLC7A11 in osteoarthritis. Front Immunol. 2023;14:1181156. https://doi.org/10.3389/fimmu.2023.1181156.
46. Chen Y, Yang X, Feng M, Yu Y, Hu Y, Jiang W. Exosomal miR-223-3p from bone marrow mesenchymal stem cells targets HDAC2 to downregulate STAT3 phosphorylation to alleviate HBx-induced ferroptosis in podocytes. Front Pharmacol. 2024;15:1327149. https://doi.org/10.3389/fphar.2024.1327149.
47. Song Y, Wang B, Zhu X, Hu J, Sun J, Xuan J, Ge Z. Human umbilical cord blood-derived MSCs exosome attenuate myocardial injury by inhibiting ferroptosis in acute myocardial infarction mice. Cell Biol Toxicol. 2021;37:51–64. https://doi.org/10.1007/s10565-020-09530-8.
48. Singh AK, Rooge SB, Varshney A, Vasudevan M, Bhardwaj A, Venugopal SK, Trehanpati N, Kumar M, Geffers R, Kumar V, et al. Global MicroRNA expression profiling in the liver biopsies of hepatitis B virus-infected patients suggests

specific MicroRNA signatures for viral persistence and hepatocellular injury. Hepatology. 2018;67:1695–709. https://doi.org/10.1002/hep.29690.
49. Dai C, Chen X, Li J, Comish P, Kang R, Tang D. Transcription factors in ferroptotic cell death. Cancer Gene Ther. 2020;27:645–56. https://doi.org/10.1038/s41417-020-0170-2.
50. Liao M, Sun X, Zheng W, Wu M, Wang Y, Yao J, Ma Y, Gao S, Pei D. LINC00922 decoys SIRT3 to facilitate the metastasis of colorectal cancer through up-regulation the H3K27 crotonylation of ETS1 promoter. Mol Cancer. 2023;22:163. https://doi.org/10.1186/s12943-023-01859-y.
51. Sun Y, Shan X, Guo J, Liu X, Ma D. CHI3L1 promotes myocardial fibrosis via regulating LncRNA TUG1/miR-495-3p/ETS1 axis. Apoptosis. 2023;28:1436–51. https://doi.org/10.1007/s10495-023-01859-9.
52. Jiang P, Wang C, Zhang M, Tian Y, Zhao W, Xin J, Huang Y, Zhao Z, Sun W, Long J, et al. Differential regulation of JAK1 expression by ETS1 associated with predisposition to primary biliary cholangitis. J Genet Genomics. 2023;50:807–12. https://doi.org/10.1016/j.jgg.2023.06.004.
53. Zhang LY, Tan Y, Luo XJ, Wu JF, Ni YR. The roles of ETS transcription factors in liver fibrosis. Hum Cell. 2023;36:528–39. https://doi.org/10.1007/s13577-022-00848-5.
54. Lee TL, Lai TC, Lin SR, Lin SW, Chen YC, Pu CM, Lee IT, Tsai JS, Lee CW, Chen YL. Conditioned medium from adipose-derived stem cells attenuates ischemia/reperfusion-induced cardiac injury through the microRNA-221/222/PUMA/ETS-1 pathway. Theranostics. 2021;11:3131–49. https://doi.org/10.7150/thno.52677.
55. Chen YC, Chuang TY, Liu CW, Liu CW, Lee TL, Lai TC, Chen YL. Particulate matters increase epithelial-mesenchymal transition and lung fibrosis through the ETS-1/NF-κB-dependent pathway in lung epithelial cells. Part Fibre Toxicol. 2020;17. https://doi.org/10.1186/s12989-020-00373-z.
56. Liu D, Wang K, Li K, Xu R, Chang X, Zhu Y, Sun P, Han X. Ets-1 deficiency alleviates nonalcoholic steatohepatitis via weakening TGF-β1 signaling-mediated hepatocyte apoptosis. Cell Death Dis. 2019;10:458. https://doi.org/10.1038/s41419-019-1672-4.

Publisher's note